BLADE PITCH & OFFSET EFFECTS ON A VERTICAL AXIS WIND TURBINE

THE EFFECTS OF BLADE PITCH AND MOUNT POINT OFFSET ON VERTICAL AXIS WIND TURBINE PERFORMANCE

By

ANDRZEJ FIEDLER, B. Eng.

A Thesis

Submitted to the School of Graduate Studies

In Partial Fulfillment of the Requirements

For the Degree

Master of Applied Science

McMaster University

MASTER OF APPLIED SCIENCE (2009) McMaster University

(Mechanical Engineering) Hamilton, ON

TITLE: The Effects of Blade Pitch and Mount Point Offset on Vertical Axis Wind Turbine Performance

AUTHOR: Andrzej Fiedler, B. Eng. (McMaster University)

SUPERVISOR: Dr. Stephen Tullis

NUMBER OF PAGES: xvi, 99

ABSTRACT

Small scale Vertical Axis Wind Turbines (VAWTs) show potential for urban rooftop installations where they can capture the highly unstable, turbulent wind flow patterns which are typical in an urban environment. Being axisymmetric, they are omni-directional turbines which respond well to changes in wind direction, unlike their horizontal axis counterparts. Wind tunnel experiments were performed on a small scale, 2.5m diameter by 3m high, 3 bladed H-Darrieus VAWT. The effects of blade preset pitch and blade mount-point offset were investigated. Local flow visualizations were observed on the inner surface of a blade near the lower strut by recording video of the behaviour of Mylar tufts during turbine operation for comparison with a 2-D Computational Fluid Dynamic (CFD) model. Experimental data is presented for a range of tip speed ratios, at a nominal wind velocity of 10m/s for both blade pitch and blade offset tests.

The results of the blade preset pitch tests indicate performance increases with increasing toe-out pitch, to a limit, followed by a sharp decrease in performance as toe-out is continually increased. Performance decreases were experienced for all toe-in pitch presets. Identical behaviour was seen with experiments involving blade mount-point offsets which were geometrically equivalent to blade pitch presets. Results of tuft flow visualization tests indicate the regions during which the blade is experiencing reversed flow, and compare well with velocity vector data obtained from CFD simulations. The duration the inner blade surface experiences full stall is observed to decrease with the increase of toe-out preset pitch. Incipient stall is observed to be delayed as blade tip speed

ratio is increased. Thrust curves are also presented and indicate a decrease in upwind pass and increased downwind pass performance as toe-out is increased. As the tip speed ratio is increased, the interaction of the blade with its shed vortex from the upwind pass is diminished. This investigation shows that high solidity VAWTs are sensitive to relatively small changes in blade preset pitch and mount point offset and therefore care should be taken when designing turbine blades so as to avoid a toe-in condition that could adversely affect turbine performance.

ACKNOWLEDGEMENTS

First and foremost I would like to express my gratitude to my supervisor Dr. Stephen Tullis, for providing me with a research opportunity in an exciting and interesting field. His knowledge and expertise were instrumental in the making of this thesis, and his patience and support allowed for a very amicable working environment. One could not ask for a better supervisor.

The assistance from my colleagues at McMaster University's Vertical Axis Wind Turbine Research Group, namely Rafael Bravo, Kareem Aly, Stephen Kooiman, Kevin McLaren and Shawn Armstrong, was instrumental in realizing the goals of my thesis, and their help and support is much appreciated.

My sincerest appreciation goes out to the many faculty members in McMaster's department of Mechanical Engineering, specifically the members of the Mechanical Engineering Machine Shop; Joe Verhaeghe, Dave Schick, Ron Lodewyks, Jim McLaren, Mark McKenzie, and J.P. Talon for the technical assistance and tools to assist me in manufacturing many different turbine components.

I am thankful for the financial support from Ontario Centres for Excellence, and Cleanfield Energy, without whom this research would not have been possible.

I would also like to thank my friends and family; specifically my parents, who supported me throughout my entire university career and whose love and support made this endeavour an enjoyable and unforgettable experience.

TABLE OF CONTENTS

LIST OF FIGURES

LIST OF TABLES

NOMENCLATURE

ENGLISH CHARACTERS

a	blade mount-point location, or offset; measured along chord line from leading edge [mm]
AR	aspect ratio – defined as the longer dimension of the height and width of the turbine divided by the shorter dimension
c	turbine blade chord length [mm]
Cp	coefficient of performance; non-dimensional ratio of turbine power to available wind power
D	turbine diameter [m]
L	blade length [m]
N	number of turbine blades
P_{net}	net turbine power available [W]
r	turbine radius [m]
Re	Reynolds number based on airfoil chord length
S	turbine swept area (projected area for VAWTs) [m^2]
T	torque generated by a single blade at a given orbital location [Nm]
$\vec{U}$	turbine incident wind velocity vector [m/s]
$\vec{U}_{\infty}$	nominal incoming wind velocity vector [m/s]
$\vec{U}_{rot}$	wind component due to turbine rotation [m/s]
x	location on blade surface measured along chord line [mm]

GREEK CHARACTERS

α angle of attack (AOA); angle between incident wind vector U and chord line [degrees]

α_0 zero nominal wind angle of attack (AOA) [degrees]

β blade preset pitch angle; angle between the blade chord and the tangent to the swept arc at the mount-point [degrees]

ϵ inverse tip speed ratio, non-dimensional ratio of nominal wind velocity to turbine blade speed

λ tip speed ratio (TSR), non-dimensional ratio of turbine blade speed to nominal wind velocity

ρ air density [kg/m^3]

σ turbine solidity, non-dimensional ratio of total turbine blade area to turbine swept area

θ turbine orbital position [degrees]

ω turbine angular velocity [rad/s]

ABBREVIATIONS

AOA	Angle of attack
BSR	Blade speed ratio
CFD	Computational fluid dynamics
NRC	National Research Council
RPM	Revolutions per minute
TSR	Tip speed ratio
HAWT	Horizontal axis wind turbine
VAWT	Vertical axis wind turbine

CHAPTER 1: INTRODUCTION

1.1 THESIS STATEMENT

Experimental wind tunnel tests and numerical computational fluid dynamics analyses were performed on a vertical axis wind turbine to examine the relationship between blade preset pitch and blade mount point offset and their effects on overall turbine performance.

1.2 MOTIVATION

With the increasing economic and environmental costs of more traditional sources of energy such as oil, coal and nuclear, the demand for alternate forms of renewable energy, especially wind power, has become more prominent. On a smaller scale, wind turbines situated in urban environments are becoming more popular with cottagers, homeowners, and local businesses as a means of offsetting their current energy demands, with some users going off the grid altogether.

Wind turbines exist in two main types: the more common horizontal axis wind turbine, and the Vertical Axis Wind Turbine (VAWT), which is most commonly seen as either a troposkein shape Darrieus VAWT, or as a straight bladed H-Darrieus variation (see Figure 1-1). Although both horizontal and vertical axis wind turbines share the fundamental similarity of generating electricity based on the principles of aerodynamic lift, they each have their advantages and disadvantages. The selection of the most appropriate wind turbine type will be ultimately dependent on its potential location and the associated wind flow patterns.

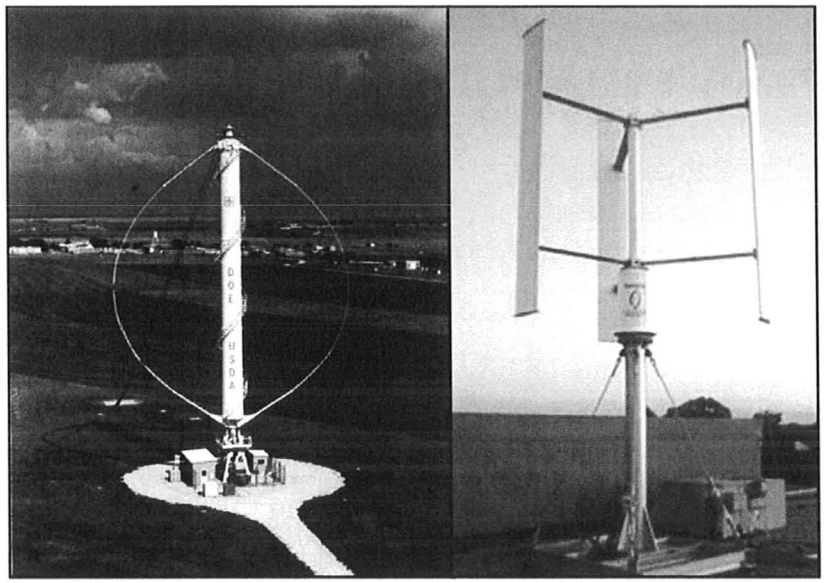

Figure 1-1: A Sandia 34m Darrieus VAWT (left) and a 3m Cleanfield V3.5 H-Darrieus (right) (Cleanfield, 2009; Sandia, 2008)

Horizontal axis wind turbines are the most common commercial wind turbine type, and resemble a traditional windmill or propeller in their appearance. They are known to be slightly more efficient than their vertical counterparts; however, they are not without their disadvantages. Mimicking a vertical cylinder, the axisymmetric nature of a VAWT allows for wind energy extraction during conditions of rapidly varying wind direction, and their base mounted generator location permits relatively easy maintenance, making it a more suitable design for small scale urban installations as compared with traditional horizontal axis turbines which require their plane of rotation to be oriented orthogonally to the oncoming wind flow. VAWTs also have the added benefit that they typically operate at lower tip speed ratios (TSR) than horizontal axis wind turbines, and the entire portion of the blade travels at the same rotational velocity. From both vibration and

particularly noise perspectives these qualities are attractive, since both noise and vibration are dependent on the velocity of the turbine blades. Wind turbines are commonly classified according to their solidity, σ, which is the ratio of total blade area to rotor projected area. The small scale, high solidity, Cleanfield V3.5 prototype vertical axis wind turbine that is the focus of this study is shown in Figure 1-2.

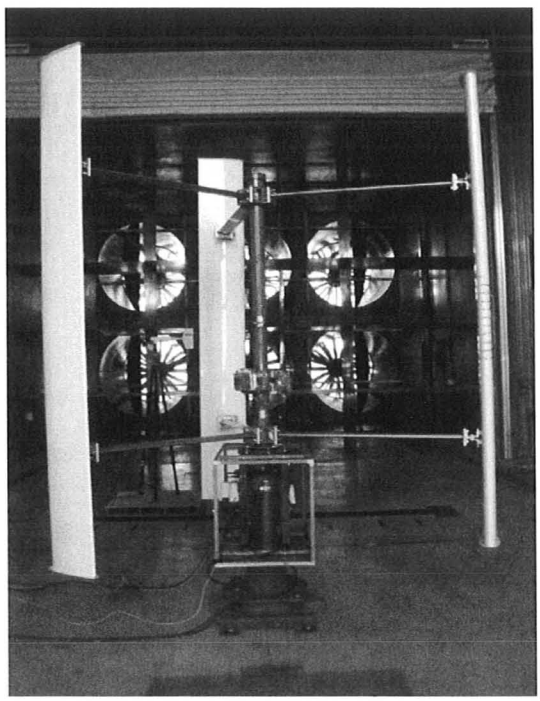

Figure 1-2: Experimental prototype of the Cleanfield V3.5 VAWT seen in the University of Waterloo open air wind tunnel facility in Waterloo, ON.

Although research has been done in the field of large scale (>50 kW) vertical axis wind turbines, comparatively little work has been performed in the field of high solidity, small scale VAWTs. Furthermore, the low solidity nature of larger scale VAWTs did not warrant the investigation of blade preset pitch and mount point offset effects on turbine

performance; however these considerations become more important as the solidity increases and the range of angles of attack (AOA) over the surface of the blade increases. Understanding the relationship between blade preset pitch and blade mount point offset, and their effects on turbine performance, are essential in the development of high solidity vertical axis wind turbine blades from the structural, vibrations, and performance points of view, and it is due to the current deficiency of this knowledge that this study was performed.

1.3 Objectives

The objectives of this research are to develop an understanding of the effects of the passive modifications of blade preset pitch and blade mount point offset on overall turbine performance. While documented literature pertaining to larger scale Darrieus VAWTs exists, there is relatively little in the area of VAWT blade design, in particular for small scale turbines. The complex nature of the flow in the presence of a vertical axis wind turbine typically requires an iterative process for optimizing the turbine blade profile. Owing to the symmetrical nature of a vertical axis wind turbine, it has been commonly assumed that a symmetrical blade profile would be most adequate to extract energy on both the upwind and the downwind blade passes. The low cost, relative ease of manufacture, and well known blade performance attributes make the symmetrical airfoil a desirable candidate. While this is not an unreasonable initial configuration for most low solidity vertical axis wind turbines, whose blades may be modelled as a single point at the end of the blade strut, higher solidity turbines will begin to experience flows over the

blade which may warrant a different blade profile for increased turbine performance. Therefore, in an attempt to add to the field of vertical axis wind turbine blade design, it is the purpose of this study to quantify the effects of simple passive changes in symmetrical blade profile orientation; namely the blade preset pitch, and the blade mount point offset, and to determine their relationship to one another and to turbine performance.

1.4 Thesis Layout

This thesis is composed of six chapters comprising an introduction, and four technical chapters which outline the topic of research and a conclusion. The introduction describes the motivation and objectives of the current research and contains an outline of the layout of the thesis. Chapter 2 introduces the reader to some technical background information pertaining to vertical axis wind turbines in order to establish a foundation for the results and discussion that are presented later. This chapter also presents a comprehensive review of the current state of the literature relating to this study. Chapter 3 is a more in depth discussion pertaining to the theory behind blade preset pitch and blade mount point offset in low and high solidity turbines and discusses the numerical (CFD) modelling used. In Chapter 4, the experimental apparatus that was the subject of the tests in this study is presented. An explanation of the modifications that were made to the turbine from its prototype state to its testing configuration is given, and is accompanied by a brief description of the control system and the adapters that were created to adjust the blade preset pitch and mount point offset. The results from the experimental wind tunnel tests, together with those performed using 2-D CFD analysis are discussed in

Chapter 5. The conclusions and scientific contributions that resulted from the aforementioned tests are summarized in Chapter 6.

An additional section is provided at the end of the thesis in Appendix A that outlines an improved method for calculating the frictional and drag losses associated with the different shaft/strut/blade combinations which were used in the experimental testing.

CHAPTER 2: BACKGROUND AND LITERATURE REVIEW

This chapter commences with a discussion on general theoretical principles relating to all wind turbines, followed by an in depth explanation of the principles of operation of a vertical axis wind turbine, and ending with a commentary on blade preset pitch and blade mount point offset theory including an examination of the existing applicable research pertaining to small scale VAWTs.

2.1 VERTICAL AXIS WIND TURBINE OPERATION

Wind turbine performance is primarily characterized by the coefficient of performance, *Cp*, which is given by:

$$Cp = \frac{P_{out}}{0.5\rho U_{\infty}^{3} S} \tag{2-1}$$

and is a non-dimensional measure of the turbine power output. The turbine tip speed ratio (abbreviated here as TSR), is the ratio of turbine blade speed to the nominal wind velocity and is defined as:

$$\lambda = \frac{\omega r}{\vec{U}_{\infty}} = \frac{\vec{U}_{rot}}{\vec{U}_{\infty}} \tag{2-2}$$

In distinguishing between different turbine configurations, two common parameters include the chord-radius ratio (*c/r*), and the ratio between the total blade area and the turbine swept area (projected area for VAWTs), known as the solidity, and defined as:

$$\sigma = \frac{NcL}{S} = \frac{Nc}{D} \tag{2-3}$$

for and H-Type VAWT. The specification of turbine geometrical parameters, including blade profile, turbine size (radius), and blade pitch/offset, is dependant on the anticipated wind conditions in the area in question, and should be optimized for the given environment in order to maximize turbine efficiency. VAWTs work on the principle of aerodynamic lift on airfoils to generate the required torque to sustain rotation, thus due to their simple design, easy manufacturability, relatively low cost, and well documented performance parameters, symmetrical airfoil sections are the most common on these turbines.

In studying non-ducted wind turbine performance there exists a maximum theoretical turbine efficiency known as the Lanchester-Betz-Joukeosky limit, or more commonly, the Betz limit (van Kuik, 2007). The maximum possible energy that may be extracted by an infinitely thin rotor, or actuator disc, assuming no heat transfer, drag losses, incompressible flow and axial flow, was proven to be 16/27 (0.593), or 59% of the total energy available. Any deviations from the assumptions made in the derivation of the Betz limit lower the energy available in the incoming fluid, lowering the overall efficiency. Modifications to the Betz limit to account for effects of flow rotation as well as attempts at modelling a VAWT as a double actuator disc have been investigated in the past. For example, Newman (1983) modeled a VAWT as a double actuator disc and determined a maximum efficiency of 0.64, while Glauert (1935) determined turbine efficiency while accounting for flow rotation resulting from the torque imposed on the flow by the turbine, and found that the maximum efficiency increases to Betz limit asymptotically from zero with increasing turbine rotational frequency.

In order to explain the basic operation of a VAWT, a quasi-steady state analysis is often employed. A plan view of a typical VAWT that includes some important variables used to describe a turbine configuration is shown in Figure 2-1.

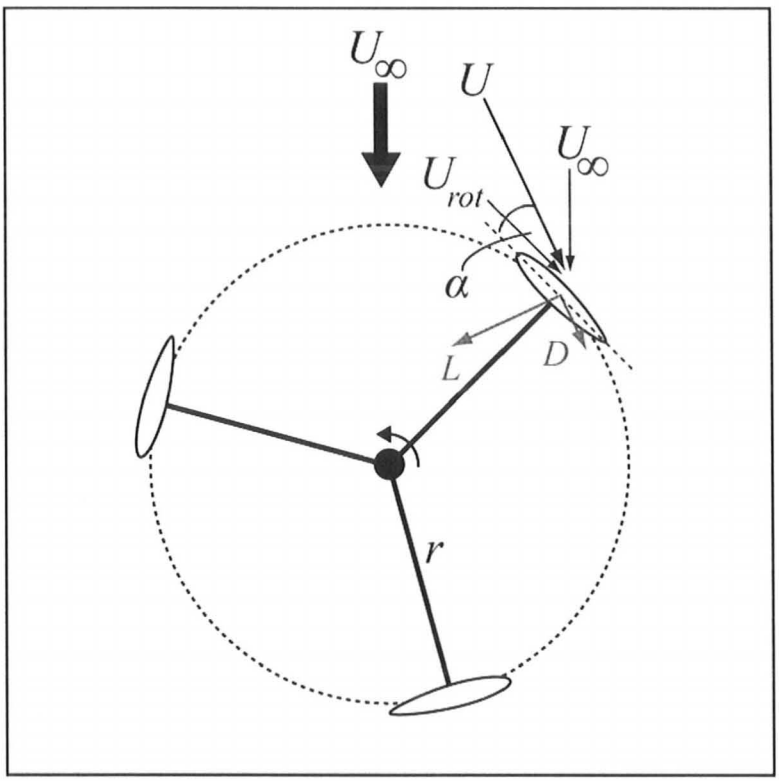

Figure 2-1: Plan view of turbine showing the ambient wind speed U_∞, rotational speed U_{rot}, relative wind speed U, the angle of attack (α), and resulting lift (L) and drag (D) forces.

Assuming a perfectly still air day ($U_\infty = 0$ *m/s*), if the turbine is set to rotate at a given angular velocity, the airfoils will experience an incident wind velocity, U_{rot}, tangent to the blades orbital path, resulting in an angle of attack, $\alpha = 0°$. During normal turbine operation a non-zero incoming wind component, $U_\infty > 0$*m/s* is present, and the vector summation of the incoming wind velocity with the rotational velocity of the blade creates a relative wind velocity, U, at a non-zero angle of attack, resulting in a lift force and a

drag force on the airfoil. When these forces (See Figure 2-1) are broken down into their respective components, the net positive thrust component contributes to the turbine rotation, whereas the fluctuating radial component can lead to turbine vibration and blade fatigue. The integration of the thrust and drag forces around the orbit of all the turbine blades results in a thrust force which determines the amount of aerodynamic power the turbine is capable of extracting from the wind.

As the nominal wind, U_∞, approaches the turbine, it is retarded and deflected around and above the turbine due to the turbine acting as a pressure obstacle in the path of the oncoming flow. The solidity of the turbine has a strong influence on the amount of upstream flow retardation. Being axisymmetric, the turbine blade extracts energy from the wind during the blades' upwind pass, and to some extent, on the downwind blade pass. For a given rotational wind component, U_{rot}, which remains constant for a constant turbine angular velocity, the variations in AOA and U are functions of only the turbine orbital position, θ, and the nominal incoming flow velocity, U_∞. As the energy is extracted on the upwind pass, the velocity of the incoming wind, U_∞ is decreased in agreement with the law of conservation of momentum, resulting in a lower AOA impinging on the downstream blade pass. Although the downwind blade pass still extracts a certain amount of energy from the flow, this amount is much lower than during the upwind pass. In the quasi-steady analysis, the lift and drag forces can be determined from readily available airfoil section lift and drag performance curves which are presented as functions of airfoil angle of attack, α, and blade Reynolds number, Re_{blade}.

The Reynolds number is a commonly used parameter in fluid dynamics and is the ratio of inertia force to viscous forces on the blade and is given in Equation (2-4):

$$Re_{blade} = \frac{\rho \vec{U}_\infty c}{\mu} = \frac{Inertia\ Force}{Viscous\ Force} \tag{2-4}$$

where ρ is the air density, c is the chord length, and μ is the dynamic viscosity of the air. The airfoil section lift and drag coefficients are presented in Equation (2-5) and Equation (2-6) as non-dimensional ratios of the lift and drag force to the dynamic force in the flow:

$$C_L = \frac{L}{0.5\rho \vec{U}_\infty^2 A} \tag{2-5}$$

$$C_D = \frac{D}{0.5\rho \vec{U}_\infty^2 A} \tag{2-6}$$

where L and D are the lift and drag forces respectively, and A is the planform area of the airfoil. Typical lift and drag performance data for the NACA 0015 airfoil, the principal profile used in the experiments presented in this thesis, is given in Figure 2-2 and Figure 2-3.

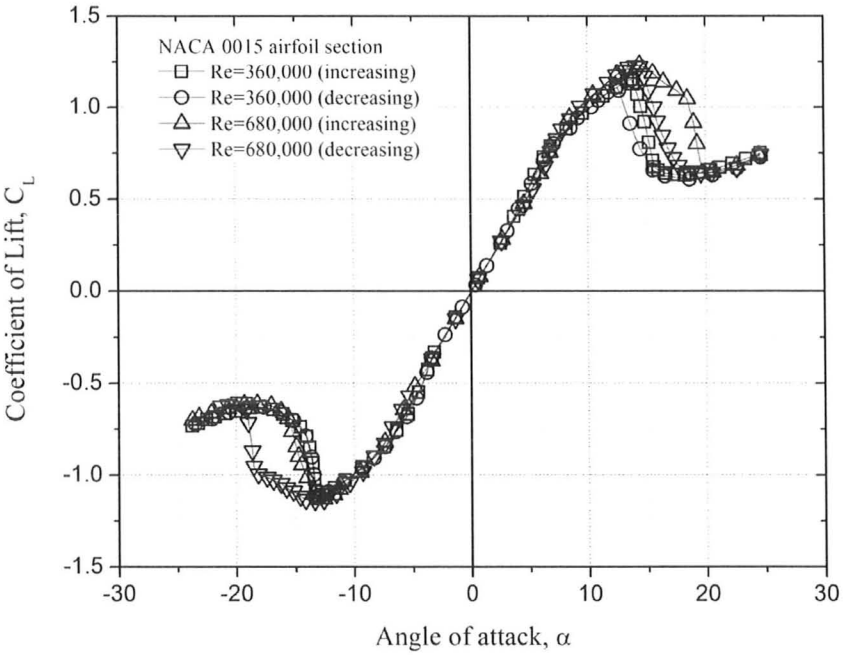

Figure 2-2: Empirical lift coefficient (C_L) data for NACA 0015 airfoil section for different Reynolds numbers (Sheldahl & Klimas, 1981).

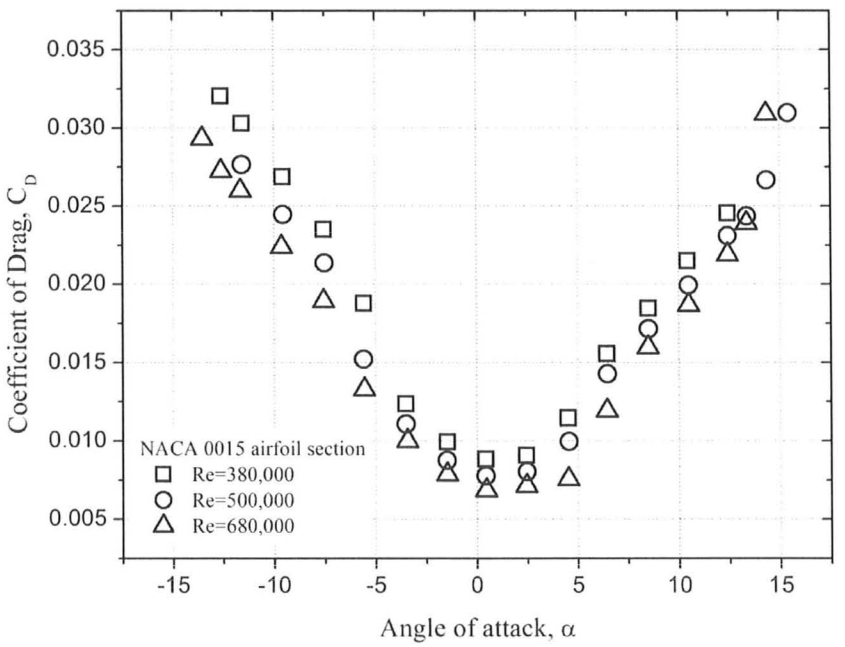

Figure 2-3: Empirical drag coefficient (C_D) data for NACA 0015 airfoil section for various Reynolds numbers (Sheldahl & Klimas, 1981).

2.2 Blade Pitch and Offset Investigations

By adjusting the preset pitch angle of the airfoil, β, – the angle with which the blade is mounted to the strut – performance changes can be expected. As wind flow passes through a turbine, the wind velocity will decrease, therefore adjusting the blade preset pitch to a toe-out configuration for a VAWT then results in a range of angles of attack (AOA) on both the upwind and downwind blade passes which are more similar than for a zero, or toe-in preset pitch configuration. It also reduces the large angles of attack seen on the upwind pass, possibly reducing the extent of dynamic stall. This pitch angle, β, is defined as positive for toe-in configurations (refer to Figure 2-4).

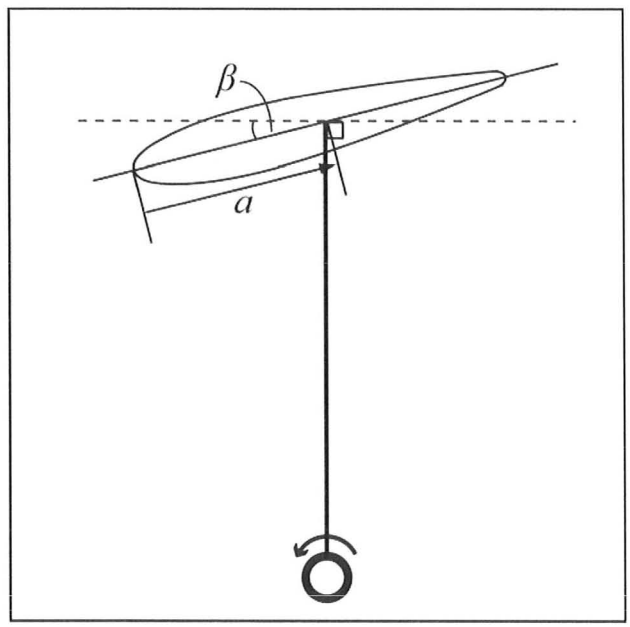

Figure 2-4: Plan view of single blade illustrating blade preset pitch, β, and mount point offset, a.

There is relatively little published literature pertaining to the effects of blade preset pitch for low solidity turbines, and the literature which exists is often cited as being an accidental change in blade pitch, as in the case of South and Rangi (1972) presented below. To the author's best knowledge, there exists no literature pertaining to blade pitch or mount point offset effects in high solidity turbines.

South and Rangi (1972) performed a wind tunnel investigation of a 4.27m diameter Darrieus VAWT at the N.R.C. 9m wind tunnel. The 2-bladed turbine had a solidity $\sigma = 0.07$, and $c/r = 0.07$. They reported increases in Cp of approximately 11% when their blades were offset from an initial pitch $\beta = -4°$ (toe-out) to a pitch of $\beta = 0°$ (see Figure 2-5). Their investigation of this phenomenon was unintentional as the blade preset pitch that was investigated resulted from errors during the blade manufacturing process.

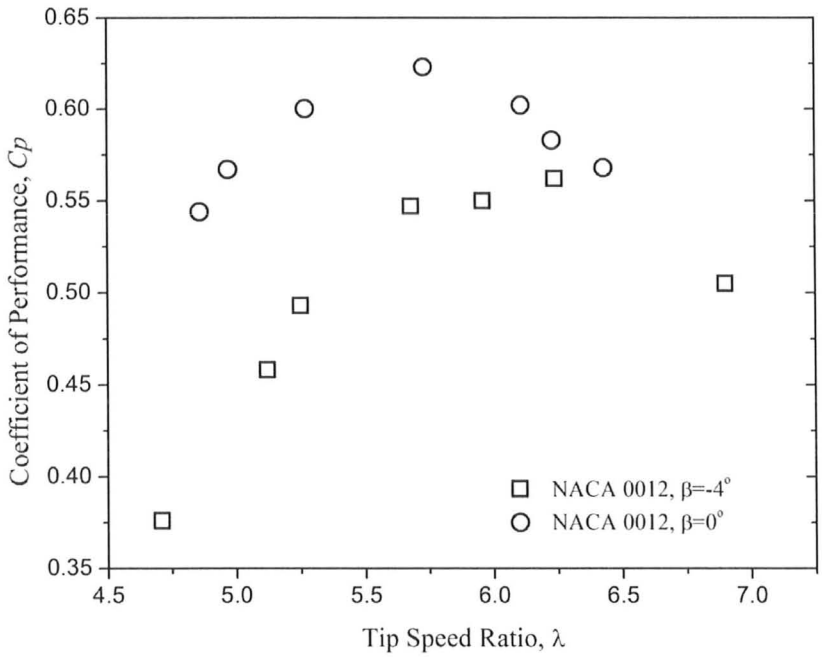

Figure 2-5: Effects of blade preset pitch on a two bladed Darrieus VAWT with NACA 0012 airfoils (South & Rangi, 1972).

Klimas and Worstell (1981) investigated the effects of blade offset on a 5m diameter Darrieus VAWT with $\sigma = 0.22$, and $c/r = 0.06$. Using a geometric analysis presented later, that relates blade offset with equivalent preset pitch, they observed power increases of approximately 3% for blade pitch offsets of up to $\beta = -2°$ (toe-out), followed by power decreases for increasingly negative values of β. They also reported lower tip speed ratios at Cp_{max} for these equivalent toe-out offsets, and higher tip speed ratios for equivalent toe-in offsets (see Figure 2-6)(Klimas & Worstell, 1981).

Low solidity turbines with a low chord-radius ratio ($c/r \leq 0.1$) can be modelled well using a Double Multiple Stream-Tube (DMST) analysis (discussed in § 3.1.1) such as one developed by Paraschivoiu (1988). Paraschivoiu (2002) reported on predictions of

the effects of preset pitch on the performance of a low solidity 50kW VAWT. Figure 2-7 indicates increases in predicted power of approximately 5% for a toe-out preset of β = -2°, versus the zero preset pitch case. For all other non-zero pitch cases, rotor performance was seen to deteriorate.

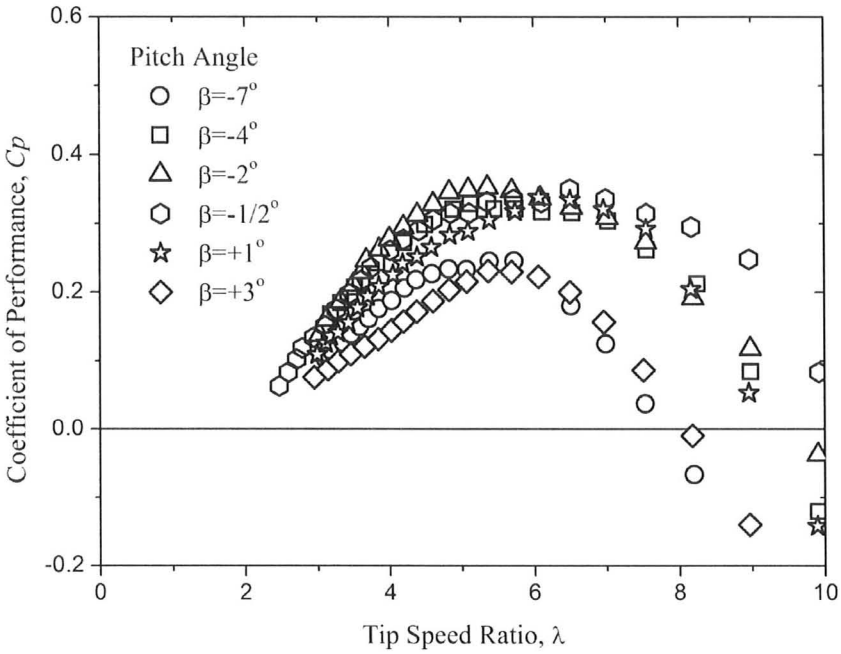

Figure 2-6: Results showing the effects of equivalent blade preset pitch resulting from mount point offset on the Sandia 5m Darrieus VAWT with two NACA 0015 airfoils (Klimas & Worstell, 1981).

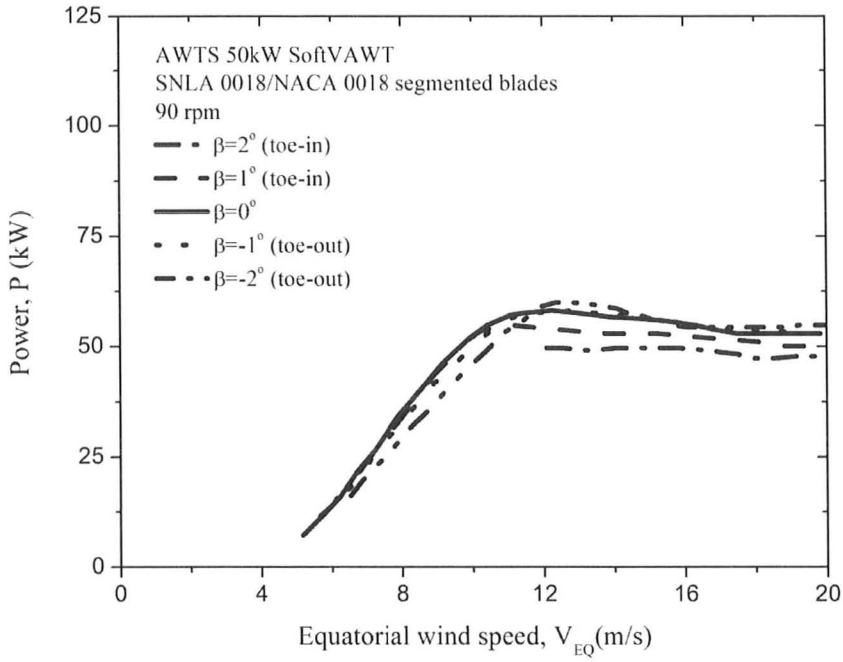

Figure 2-7: Effects of blade preset pitch on performance of 50kW VAWT (Paraschivoiu, 2002).

A small chord airfoil, mounted at a large distance from the central shaft, results in a nearly constant zero-wind angle of attack, $\alpha_0 = 0°$. That is, as the turbine is rotating on a perfectly still air day, the entire blade will see the relative airflow at $\alpha_0 = 0°$.

Complications arise when the turbine geometry involves relatively large chord length blades mounted at a relatively short radius. As the solidity increases as a result of an increased *c/r* ratio, the orbits of the leading, centre, and trailing edges of the blade differ, and modelling the entire blade as a single point experiencing a single angle of attack is no longer a suitable approximation. If the blade is mounted at mid-chord, for example, the leading edge will 'sweep' around the orbit resulting in a negative AOA for locations approaching the blade mount point, while the trailing edge will follow a 'skidding' path, resulting in a positive AOA for locations aft of the mount point. It has

been shown that as the *c/r* ratio of the turbine is increased, thus increasing the solidity, the quasi-steady nature of the turbine becomes progressively more complicated resulting from dynamic effects such as dynamic stall as well as periodic blade-vortex interaction (McLaren *et al.*, 2009). Some attempts to compensate for the effects of dynamic stall in the DMST analysis have been made by adjusting the AOA based on empirical observations (Paraschivoiu & Delclaux, 1983).

Numerical methods to compensate for the effects of this flow curvature experienced in high solidity, high *c/r* VAWTs have also been investigated in the past. For example, Migliore *et al.* (1980) used a conformal mapping technique to model symmetrical airfoils in curvilinear flow as hypothetical airfoils with a virtual camber and virtual incidence in a rectilinear flow field. Sectional airfoil data for the virtual airfoil was then used to approximate the lift and drag characteristics of the symmetric turbine blade. Also, the use of a modified stream-tube model, which assumes that a curvilinear flow over a symmetrical airfoil may be likened to a rectilinear flow over the same symmetrical blade by calculating a set of equivalent flow parameters based off a circular arc cambered airfoil, was investigated with success by Hirsch and Mandal (1984), and later by Mandal and Burton (1994). Although numerical schemes exist that attempt to compensate for the effects of flow curvature in turbine performance predictions, comparatively little numerical and experimental work has been published on the effects of blade mounting configurations in small scale, high solidity, high *c/r* VAWTs.

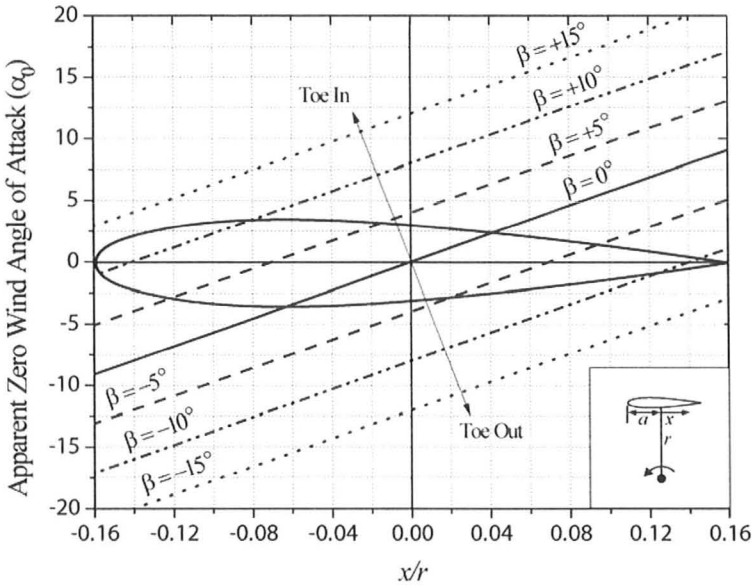

Figure 2-8: Apparent zero wind angle of attack (α_0) as a function of chord location, x/r, and preset pitch angle, β. Blade profile shown corresponds to blade with chord c = 400mm, radius r = 1250mm, mounted at a = 200mm (mid-chord).

For a VAWT of any ratio of *c/r*, the zero wind angle of attack can be determined by Equation (2-7):

$$\alpha_0 = \tan^{-1}\left(\frac{x}{r}\right) - \beta \tag{2-7}$$

where positive x is defined as the location along the blade chord from the centre of the mount point towards the trailing edge of the airfoil. This can also be found by reading the apparent AOA value at the intersection of the *x/r* position with the blade preset pitch angle, β, on Figure 2-8. The outline of the airfoil illustrates the maximum and minimum values of *x/r* for the mid-mount blade that was tested. For blades that are not mounted at mid-chord, the maximum and minimum *x/r* values will be different, and not centered around zero. From Figure 2-8, with *c/r = 400mm/1250mm* the apparent AOA at the

leading and trailing edges, with zero preset pitch is in the range $-9.1° \leq \alpha_0 \leq 9.1°$, so at any given moment the airfoil experiences AOA variations of $\Delta\alpha_0 \approx 18°$ over the chord length. This is a large amount of variation in contrast to $\Delta\alpha_0 \approx 3.6°$ that is encountered by the low *c/r* turbine in the findings of Klimas and Worstell (1981). This variation decreases even more for lower solidity turbines, so it is acceptable to model the blades of a low solidity turbine as having a constant AOA over the entire chord length.

2.3 Computational Fluid Dynamics Investigations

Detailed computational fluid dynamics simulations of the complex flow patterns associated with vertical axis wind turbines have begun to be investigated. Guerri *et al.* (2007) used a two-dimensional CFD model to determine blade loading on the turbine as well as to compare performance with existing multiple stream-tube models, with some success. However, their model is designed for relatively low solidity turbines ($\sigma = 0.16$) that can be modelled from existing vortex and stream-tube models, and would therefore be inadequate for modelling a high solidity turbine.

Computational fluid dynamics has also been used by McLaren *et al.* (2007a, 2007b) to model the flow through and around a high solidity turbine. The results of the CFD simulations showed a complex vortex rollup and shedding behaviour on the upwind blade pass, and interaction between the blades and their shed vortices on the downwind pass; phenomena that are difficult to include in quasi-static DMST models. Due to the large variation in AOA over the chord of the airfoil, a turbine with a high *c/r* is thought to be

sensitive to changes in the offset or preset pitch of its blades. Theoretically optimal, preset pitch angles may be defined that minimize 'skidding' effects and early onset stall.

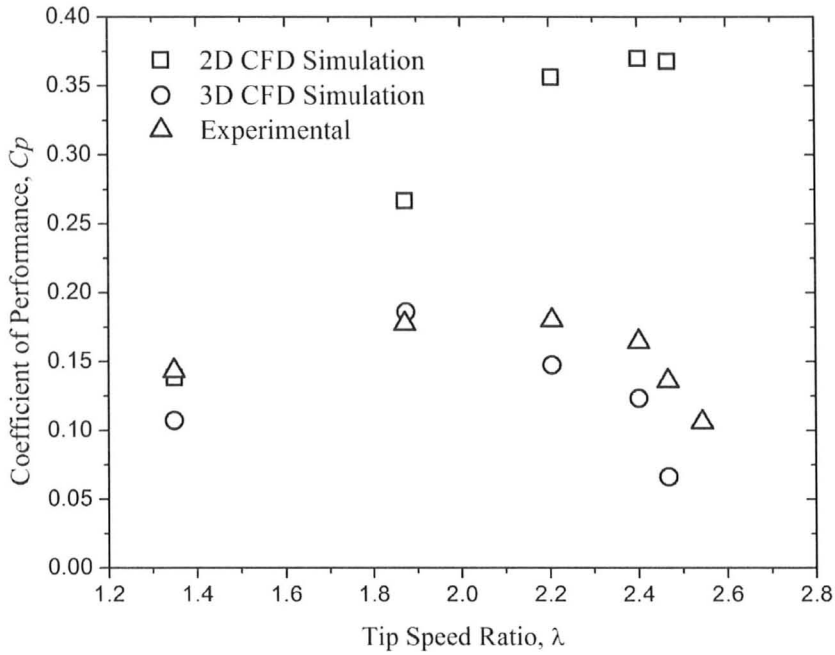

Figure 2-9: Comparison of 2-D and 3-D CFD simulations with experimental data on a small scale, high solidity VAWT for $U_\infty = 4.31m/s$. Reproduced from Howell *et al.*(2009).

Howell *et al.* (2009), very recently performed both 2-D as well as 3-D simulations on a small-scale, high solidity (2 blades $\sigma = 0.67$, 3 blades $\sigma = 1.0$) VAWT and showed that their 2-D simulation does not accurately predict wind tunnel performance data for the turbine. They attributed this to the findings obtained from their 3-D simulations which showed periodic pulsations due to wing-tip vortices as the blades were loaded and unloaded.

CHAPTER 3: VAWT MODELLING THEORY

3.1 VAWT MODELLING

The use of mathematical models to predict the outcome of experiments is desirable to minimize the time and costs required in performing the individual experiments. Numerical methods have been used in the past to predict VAWT performance; and some of their merits and shortcomings are addressed in the following sections.

3.1.1 DOUBLE MULTIPLE STREAM-TUBE MODELS

A common and relatively simple technique is the Double Multiple Stream-Tube analysis (DMST). In this context, the 'double' is a reference to the two passes a single blade makes across the incoming wind (the upwind and the downwind passes), while the 'multiple stream-tube' makes reference to the multiple vertical slices the turbine is divided into in which momentum must be conserved (see Figure 3-1).

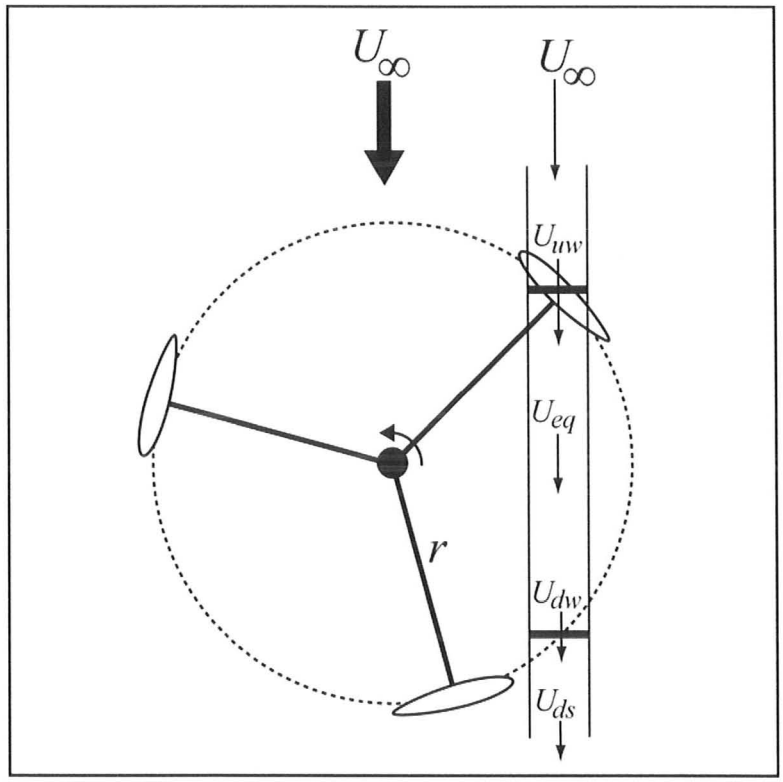

Figure 3-1: VAWT rotor geometry with typical stream-tube shown. Velocities are calculated at the upwind pass, U_{uw}, the equator, U_{eq}, at the downwind pass, U_{dw}, and downstream of the turbine, U_{ds}.

The DMST is an iterative process which combines blade element theory with conservation of fluid momentum to determine the velocity drop of the wind in a stream-tube as it passes through the turbine. It is relatively easy to implement, but given that it uses steady state wind tunnel airfoil performance characteristics, its use is limited to low solidity, low c/r ($c/r \leq 0.1$) ratio turbines, for which it is acceptable to model the blade in a quasi-steady fashion as a point at the end of a radius arm. It follows then that the calculated angle of attack is constant over the *entire* surface of the airfoil, and the aerodynamic lift and drag characteristics may be approximated using steady state wind tunnel data for the particular airfoil section. Though attempts have been made to account

for effects that are more predominant in a higher solidity turbine such as flow curvature (Mandal & Burton, 1994; Migliore *et al.*, 1980) and dynamic stall (Paraschivoiu & Delclaux, 1983), the DMST model's inherent assumptions of horizontal airflow with no consideration for flow deflection around the turbine due to its one dimensional nature, result in less than adequate performance predictions for high solidity turbines such as the Cleanfield V3.5, and therefore other methods of performance prediction are required.

3.1.2 Vortex Wake Models

Another series of numerical models include the so-called vortex models. These models assume potential flow and calculate the velocity field throughout the VAWT by measuring the vorticity in the blade wake. The turbine blades are modeled by a vortex filament, or lifting-line, whose vortex strengths are calculated from steady-state airfoil datasets. The vortex model was first introduced by Larsen (1975) to model a pitch-controlled cyclogiro turbine which operates at very low angles of attack, and thus aerodynamic stall effects were neglected. The model was extended to straight bladed VAWTs (Fanucci & Walter, 1976) and used also by Holme (1976) and Wilson (1980), but it was Strickland *et al.* (1979) who extended the model to three dimensions and incorporated stall effects. Later he made improvements to this model to include dynamic effects.

Flow curvature effects described by Migliore *et al.* (1980) were incorporated with some success by Cardona (1984). Though vortex models offer an improvement on one dimensional DMST simulations, they require significantly more computational time, and

still make significant assumptions (potential flow assumed in the blade wake, effect of viscosity on airfoil performance is determined only through empirical force coefficients) (Islam *et al.*, 2007). For these reasons, and due to the increased capability of today's computer resources, a CFD model was determined to be most suitable for use in this study.

3.2 CFD Modelling

Simulations using computational fluid dynamics were performed in an attempt to obtain a better understanding of the flow field and forces experienced by the wind turbine. Computational fluid dynamics simulations are based on using numerical techniques to solve the equations which govern the fluid motion. The domain in which these equations are applied may be discretized by the finite-difference, finite-element or finite-volume methods. The commercial CFD code used in this analysis uses the finite-volume approach, where the entire domain is partitioned into a finite number of small control volumes in which the governing equations are solved.

3.2.1 Navier-Stokes Governing Equations

The set of equations used to determine solutions to common fluid flow problems are known after their founders as the Navier-Stokes equations. For an isothermal, incompressible fluid flow, they consist of the equations for conservation of momentum, and conservation of mass (continuity). For a three-dimensional incompressible flow, the continuity and conservation of momentum are respectively,

$$\rho \frac{\partial}{\partial x_i}(u_i) = 0 \tag{3-1}$$

$$\rho \frac{\partial}{\partial t}(u_j) + \rho \frac{\partial}{\partial x_i}(u_i u_j) = -\frac{\partial p}{\partial x_j} + \frac{\partial}{\partial x_i}\left[\mu\left(\frac{\partial u_j}{\partial x_i} + \frac{\partial u_i}{\partial x_j}\right)\right] \tag{3-2}$$

3.2.2 Turbulence Modelling In CFD

The Navier-Stokes equations presented are also applicable to solving turbulent flows if the values of the fluid properties and dependent and variables are replaced by the instantaneous values. The equations can then be solved for specific boundary and initial conditions that include time-dependent quantities. To obtain mean flow parameters, an ensemble of solutions is averaged; and this process forms the basis for Direct Numerical Simulations (DNS). Determining solutions and ensemble averaging them is very expensive in terms of computational resources, thus it is most common to average the equations rather than the solutions. This is accomplished by substituting the instantaneous parameters with an average and a fluctuating component as shown below:

$$u_i = U_i + u_i', \quad p = P + p' \tag{3-3}$$

Substitution of these equations into the Navier-Stokes equations results in the continuity and conservation of momentum equations taking the following form:

$$\rho \frac{\partial}{\partial x_i}(U_i) = 0 \tag{3-4}$$

$$\rho \frac{\partial}{\partial t}(U_j) + \rho \frac{\partial}{\partial x_i}(U_i U_j) = -\frac{\partial P}{\partial x_j} + \frac{\partial}{\partial x_i}\left[\mu\left(\frac{\partial U_j}{\partial x_i} + \frac{\partial U_i}{\partial x_j}\right) - \rho\overline{u'_j u'_i}\right] \tag{3-5}$$

The additional terms found on the right hand side of the momentum equations are known as the Reynolds stresses, and introduce additional unknowns into the system of equations. This is known as the 'closure' problem in turbulent flows and various turbulence schemes exist which attempt to model these Reynolds stresses.

3.2.3 Solving the Closure Problem

Several methods exist which attempt to model the Reynolds stresses through the use of a turbulent eddy viscosity term in order to solve the Navier-Stokes equations for turbulent flows. The most basic of these methods, known as zero-equation models, involve calculating the turbulent eddy viscosity from flow variables such as the boundary layer velocity profile. Because these models do not account for convection and diffusion of turbulent energy, they are often reserved for simple flow geometries. One-equation turbulence models improve on the zero-equation models by solving a turbulent transport equation, but require a series of model constants to be tuned to the specific flow conditions. The Spalart-Allmaras model is a one-equation model which considers the transport of turbulent viscosity and thus works well on airfoils because of its ability to predict flow separation (Spalart & Allmaras, 1992).

Two-equation turbulence models include a transport equation for the turbulent kinetic energy and either the turbulence dissipation, ε, or turbulence frequency, ω, giving them the ability to account for convection and diffusion of turbulent energy and allowing them to be applied to a variety of fluid flows. Popular two-equation models include the k-epsilon, k-omega, and Shear-Stress Transport (SST) model. The first of these, the k-

epsilon model (Jones & Launder, 1972), has been demonstrated in dealing with turbulence in free-shear flows with good results, however its predictions of turbulent eddy viscosity in boundary layer flows and near wall regions are less than satisfactory, resulting in inadequate prediction of flow separation (Menter *et al.*, 2003).

In contrast, the k-omega turbulence model (Wilcox, 1993) handles turbulence in boundary layer flows well, however its over sensitivity to turbulence in the free-stream flow prevents it from accurate flow separation predictions (Menter, 1992). In order to overcome the shortcomings of the two previous models, a hybrid blend of the k-epsilon and k-omega models, known as the SST model was developed (Menter, 1994). This model uses a blending function to switch from the k-epsilon to the k-omega model as it approaches a near-wall region and is described in more detail in §3.3.1.

3.3 VAWT CFD Model Description

The CFD model used for the simulations was a slightly modified version of a 2D model originally developed by McLaren *et al.* (2007a, 2009). Though the 2D model may not accurately predict absolute magnitudes of flow variables, it is hoped that the physics of the flow and general trends in performance may still be examined. The highly coupled, non-linear equations presented in the preceding section were solved using the commercially available Ansys CFX CFD code. The solution of the unsteady Reynolds Averaged Navier-Stokes (URANS) equations uses fully-implicit discretization scheme with a time-step size equivalent to a $\theta = 1.0°$ rotation of the turbine. The time-step size was taken from the time-step independence tests carried out by McLaren *et al.* (2009).

The two dimensional computational domain was used because of the extensive computational resources that would be required to simulate the turbine in three dimensions. The entire numerical domain consists of a large stationary domain that is 20m wide by 35m long which contains a circular rotating domain 7m in diameter located 10m from the inlet. The rotating domain contains the three blade profiles located at a radius of 1.475m from the centre of a 0.1m diameter circular shaft (see Figure 3-2), and is joined to the stationary domain by means of a sliding mesh interface in order to maintain information transfer across the moving boundary. The size of the domains was determined by incremental changes to the size such that the edges of the stationary domain were far enough from the turbine blades that they did not affect the pressure field and therefore the loads on the blades. The size of the rotating domain was determined such that the fine mesh surrounding the blades remained with the blades as the domain rotated. The details of this analysis may be found in McLaren *et al.* (2009).

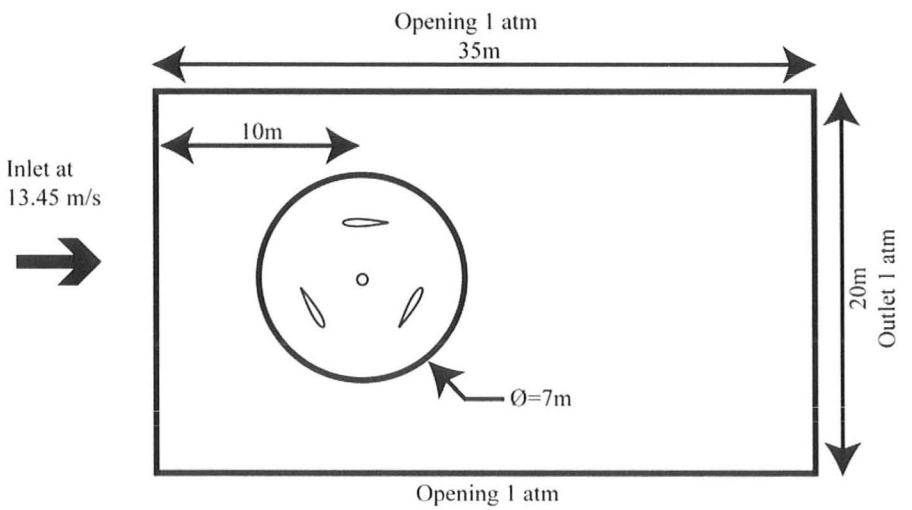

Figure 3-2: Plan view of the 2-D numerical domain used for the CFD simulations (Figure not to scale – airfoils enlarged for clarity).

The inlet flow velocity was set at U_∞ = 13.45m/s normal to the inlet boundary with a turbulence intensity of 5%. The sides and the outlet of the stationary domain were specified to have turbulent properties with zero gradients and were set as 'openings' such that they could accept flow into or out of the domain. Blade and shaft surfaces were modelled as smooth walls with non-slip surfaces. The entire domain was initialized with the same conditions that were applied to the inlet surface.

3.3.1 The SST Turbulence Model

The two-equation Shear-Stress Transport (SST) turbulence model (Menter, 1994) was applied to the simulations in order to take advantage of the k-ω model behaviour near the walls in the boundary layer while maintaining the functionality of the k-ε (Jones & Launder, 1972) model in the free-stream, thereby avoiding the issues of k- ω sensitivity to inlet free-stream turbulence properties (Wilcox, 1993). Though the one-equation Spalart-Allmaras model may have been suitable, use of the more versatile SST model had already been selected by McLaren *et al.* (2009) due to its success in horizontal axis wind turbine applications, its ability to deal with strong adverse pressure gradients.

The two transport equations of k and ω, which form the basis of the SST transition model, are given below:

$$\frac{\partial k}{\partial t} + U_j \frac{\partial k}{\partial x_j} = P_k - \beta^* k\omega + \frac{\partial}{\partial x_j}\left[(\upsilon + \sigma_k \upsilon_T)\frac{\partial k}{\partial x_j}\right] \tag{3-6}$$

$$\frac{\partial \omega}{\partial t} + U_j \frac{\partial \omega}{\partial x_j} = \alpha S^2 - \beta \omega^2 + \frac{\partial}{\partial x_j}\left[(\upsilon + \sigma_\omega \upsilon_T)\frac{\partial \omega}{\partial x_j}\right] + 2(1 - F_1)\sigma_{\omega 2}\frac{1}{\omega}\frac{\partial k}{\partial x_i}\frac{\partial \omega}{\partial x_i} \quad (3\text{-}7)$$

The turbulence production limiting term, P_k, is defined as:

$$P_k = min\left(\tau_{ij}\frac{\partial U_i}{\partial x_j}, 10\beta^* k\omega\right) \quad (3\text{-}8)$$

and the turbulent eddy viscosity is computed from:

$$\upsilon_T = \frac{a_1 k}{max(a_1\omega, SF_2)} \quad (3\text{-}9)$$

Each of the constants is a blend of an inner (ϕ_1) and outer (ϕ_2) constant that are blended using:

$$\phi = \phi_1 F_1 + \phi_2(1 - F_1) \quad (3\text{-}10)$$

where F_1 is the blending function that changes from 0 to 1 as the distance to the wall decreases. Additional functions are given by:

$$F_2 = \tanh\left[\left[max\left(\frac{2\sqrt{k}}{\beta^*\omega y}, \frac{500\upsilon}{y^2\omega}\right)\right]^2\right] \quad (3\text{-}11)$$

$$CD_{k\omega} = max\left(2\rho\sigma_{\omega 2}\frac{1}{\omega}\frac{\partial k}{\partial x_i}\frac{\partial \omega}{\partial x_i}, 10^{-10}\right) \quad (3\text{-}12)$$

$$S = \sqrt{2S_{ij}S_{ij}} \quad (3\text{-}13)$$

The coefficients in the previous equations are outlined in Table 3-1:

a_1	0.31
α_1	5/9
α_2	0.44
β_1	3/40
β_2	0.0828
β^*	9/100
σ_{k1}	0.85
σ_{k2}	1
$\sigma_{\omega 1}$	0.5
$\sigma_{\omega 2}$	0.856

Table 3-1: Coefficients for the SST Turbulence Model.

3.4 CFD Mesh Validation

The mesh specifications for both the stationary and rotating domains were initially taken from those specified in McLaren *et al.* (2009) because satisfactory results from mesh independence tests were seen. Problems arose when attempting to mesh the rotating domain when a blade preset pitch was applied. The fine mesh spacing that was specified around the blade would not always mesh properly, resulting in an intermittent boundary layer mesh along certain parts of the blades. In order to rectify this problem, the rotating domain was divided into three identical 'slices' spanning a 120° arc, onto which the existing mesh specifications were subsequently applied. In essence, a single slice of the rotating domain was meshed (see Figure 3-3) and then duplicated twice, resulting in a single rotating domain comprised of three identical meshes glued at their joining interfaces.

The nodal spacing along the adjoining edges was specified so that when the mesh was duplicated, the nodes on one edge would match up with the corresponding node on the adjoining edge. Constant edge spacing was specified along the edges such that the spacing was of the order of the unstructured mesh between the shaft and the blade. It is acknowledged that although the grid resolution along these edges may be unnecessarily fine, it is emphasized that the primary objective in using the CFD model was to compare *trends* that were predicted to those observed in experiments. The number of inflated layers on the boundary was increased from 38 to 48 in order to lower the average y^+ of the first node from the blade surface. There are 182,000 nodes in each rotating domain slice, and the fine mesh near the airfoil results in 941 nodes along the surface of the blade, with the first node occurring at an average of $y^+ < 0.5$ and a maximum of $y^+ = 2.67$.

In total, there are 547,000 nodes in the entire rotating domain, The number of unstructured nodes in the stationary domain was increased from 5,700 to 21,000 nodes since it is a relatively small increase compared to the total number of nodes, thus adding little to the total simulation time; and results in a more detailed representation of the fluid flow field around the turbine.

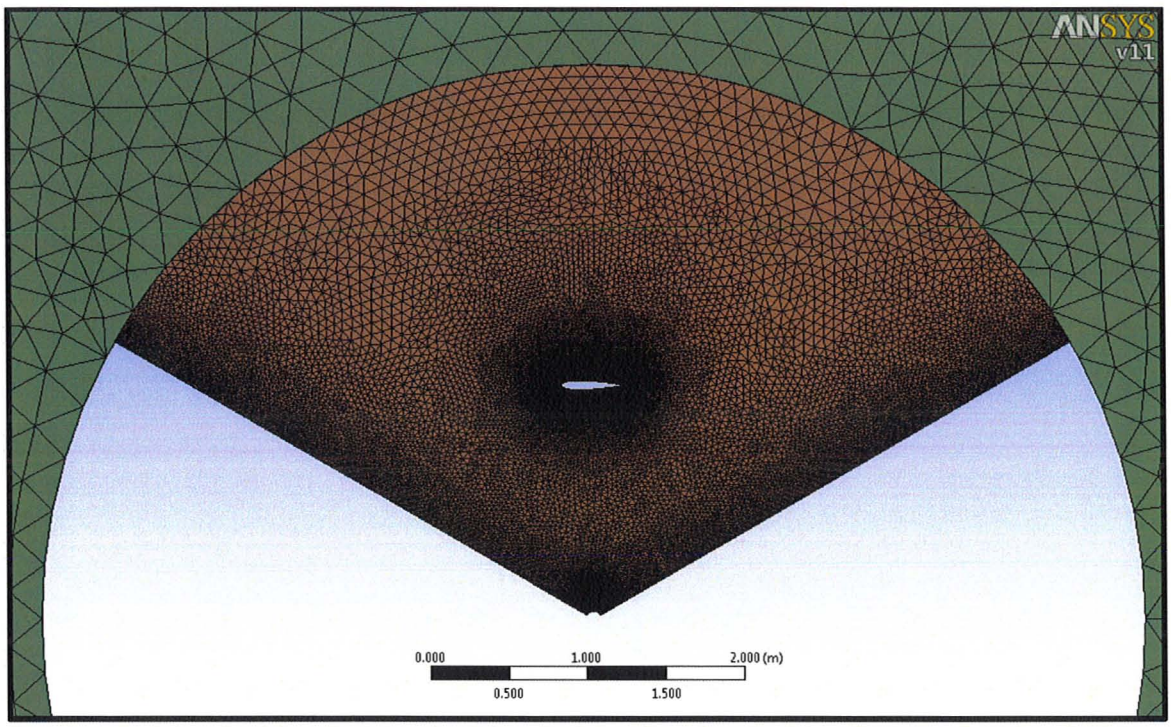

Figure 3-3: Close-up of a typical 120° rotating domain mesh (brown). Coarse unstructured mesh seen in stationary domain (green).

Due to the relatively significant change in meshing the rotating domain, a mesh independence test was performed; however, since the mesh specifications were based off those originally developed by McLaren *et al.* (2009), the finest mesh that was tested contained only 1.4 times as many nodes as the mesh used by McLaren *et al.* (2009). In these tests, the mesh denoted by B is the base case mesh which contained as many nodes as the mesh specified by McLaren *et al.* (2009). A table outlining the different meshes and their node distributions and total number of nodes is shown in Table 3-2.

Mesh refinement involved varying the number of inflated boundary layers from the base case (B) number. The stationary domain mesh remained the same throughout all tests with the exception of mesh D; where the number of stationary mesh nodes was

increased from 5700 to 21,000. This stationary mesh was tested with the C rotational mesh because it was deemed that particular rotational mesh was the most adequate for the rotational domain from both solution-accuracy and time-to-solve standpoints.

Mesh Designation	Stationary Nodes	Rotational Nodes	Total Nodes
A	5696	139694	424778
B	5696	160696	487784
C	5696	182346	552734
D	21086	182346	568844
E	5696	225146	681134

Table 3-2: Node distribution for the various meshes that were tested.

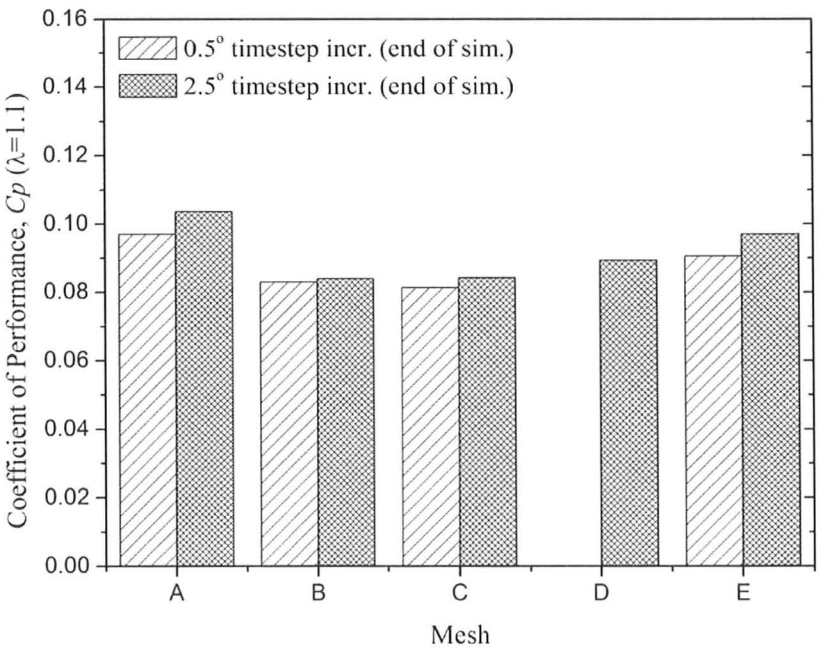

Figure 3-4: Cp for the various meshes at λ = 1.1 for both 0.5 and 2.5 degree increments (where available).

Figure 3-4 shows the variation of Cp with varying mesh, with increasing number of nodes from left to right. It is clear from the results that decreasing the time-step (the degree increment) does not provide any substantial change in performance, but comes with a massive increase solving time as shown in Figure 3-5, therefore mesh D was only tested using the 2.5° time-step interval.

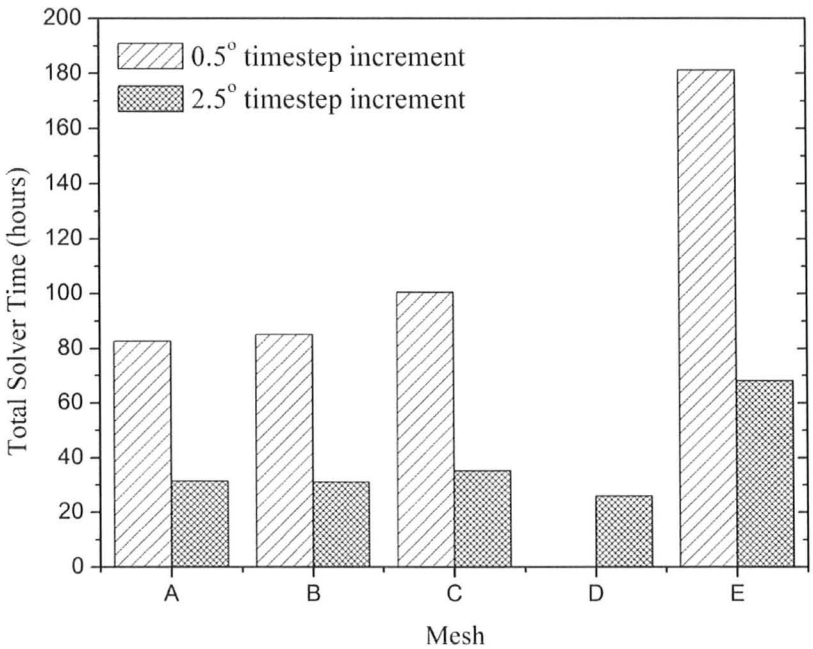

Figure 3-5: Comparison of total time, in hours, to solve simulations for varying time-step size.

In order to achieve adequate performance with the SST turbulence model, an average $y^+ < 1$ at the first node of the blade surface was required, and was achieved with meshes C, D, and E. Given that the difference in *Cp* values between the base-case (B) and the finest mesh (E) is less than 10%, and that mesh 'D' yielded the solution in the least amount of time while providing a finer resolution in the stationary domain, the specifications for mesh 'D' were used for the CFD tests presented in this thesis.

CHAPTER 4: EXPERIMENTAL APPARATUS

4.1 GENERAL VAWT SYSTEM SETUP

The experiments outlined in this thesis were all performed on an early prototype of a Cleanfield V3.5 vertical axis wind turbine. The turbine is an H-Darrieus and has a nominal height and width of 3m and 2.5m respectively. It consists of three airfoils mounted at 120° intervals, although provisions exist which allow the operation of the turbine with two blades spaced at 180°. The blades have a span of exactly 3m, and each is mounted to the central shaft by means of two support struts, which are attached one quarter of the blade span from either end. Due to the turbine being in its prototype stages, changes in turbine strut design were usually accompanied by changes to the turbine shaft design, and therefore the exact dimensions of the various strut and shaft combinations have been omitted from this section and instead the turbine radius, measured from the centre of the shaft to the chord line at the blade mount point will be given when discussing the results in Chapter 5. The experiments presented here used two different styles of struts: steel square tube struts which were fitted with fibreglass fairings, and extruded aluminum streamlined struts. Though their construction is different, their aerodynamic profiles are very similar.

The turbine blades used in this study are symmetrical NACA 0015 and NACA 0021 profile blades made of fibreglass laid up in a mould. The two profiles are based on a 450mm chord length whose trailing edge was shortened and rounded with a 10mm radius at the 400mm location (see Figure 4-1). This was done from a manufacturing standpoint

in an effort to promote a stronger bond along the trailing edge of the blade. The location of the blade mount points along the chord is measured from the leading edge of the blade and is referred to using the parameter *a*. There are two sets of NACA 0015 profile blades, differing only by the chord-wise location of the mount point, either being $a = 200mm$ or $a = 150mm$. The single set of NACA 0021 blades has a mount point at $a = 145mm$.

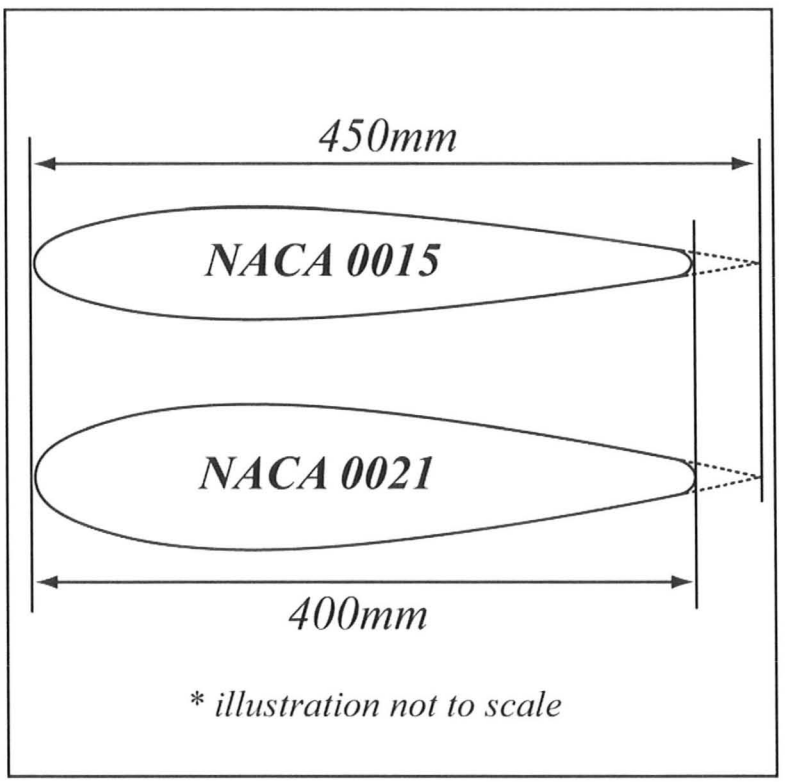

Figure 4-1: Comparison of NACA 0015 and NACA 0021 profiles. Airfoils were manufactured by truncating a longer chord profile with rounded trailing edge.

The turbine shaft is composed of two main components: An outer rotating portion to which the struts are bolted, and an inner stationary shaft. The generator is also designed so that its outer portion (rotor) rotates about a stationary inner core (stator). Thus the turbine inner shaft may be rigidly connected to the generator stator, while the

rotating outer portion of the shaft is mated to the generator rotor with a coupling that allows for torque transfer.

The purpose of the generator in this setup is mainly to provide a structural support to which the turbine shaft is connected. There are six bolts around the outer periphery at the base of the generator, spaced at 60° increments, that pass in front of a capacitive proximity sensor (TURCK model Ni-4-M12-APX6-H1141) when the turbine is operating, and are used for measuring the turbine RPM. The electrical components of the generator are not used for the purposes of energy extraction, however the generator leads may be shorted to bring the turbine to a controlled stop should the need arise. The entire generator unit is mounted to a 0.75m high steel pedestal. Also mounted to the pedestal is a large rectangular steel frame that holds all necessary instrumentation (see Figure 4-2).

A steel brake disc is sandwiched between the top of the generator and the coupling to the turbine shaft, and a floating hydraulic caliper is used to apply a brake load to control the turbine rotational speed. The floating caliper is mounted to a linear bearing such that when brake pressure is applied, the caliper pushes up against a linear load cell (Transducers Inc #T363-500-20P1) (see Figure 4-3). In this manner, the turbine torque can be easily and reliably calculated, and if the rpm is known, the net available power may be calculated. A modified commercially available, PWM-controlled, electro-hydraulic trailer brake actuator (BrakeRite model 5237006) is used to apply the necessary pressure to the floating caliper. Power to the electro-hydraulic actuator is provided by an external 12V lead-acid battery.

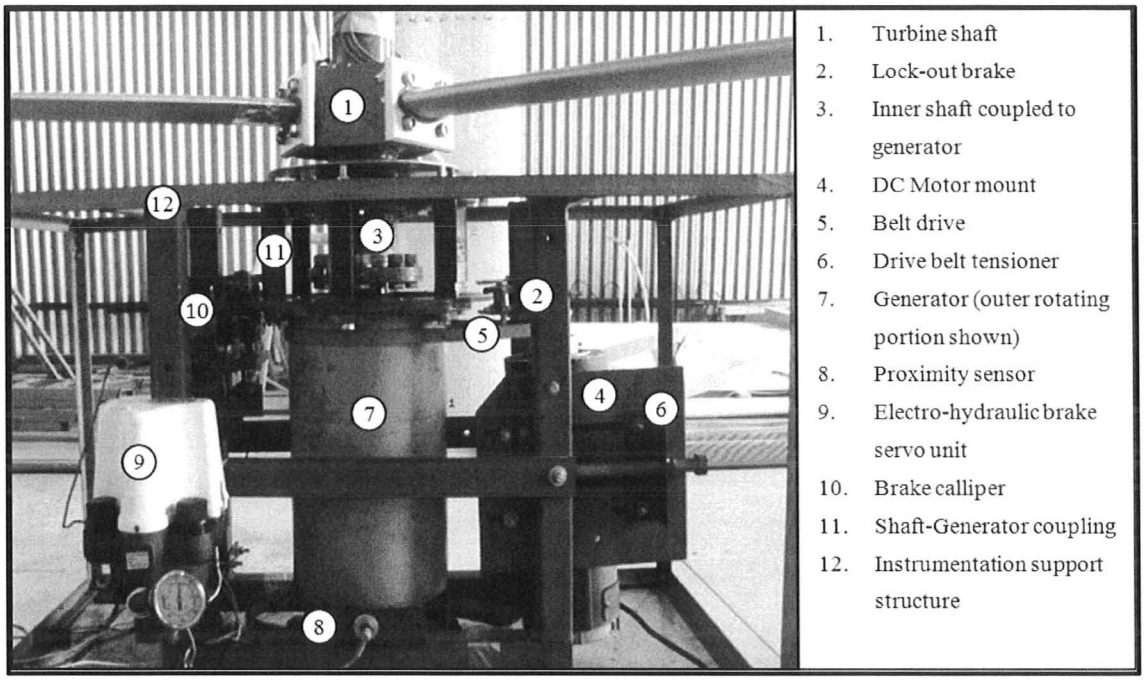

Figure 4-2: Side view of the generator and instrumentation on the experimental VAWT

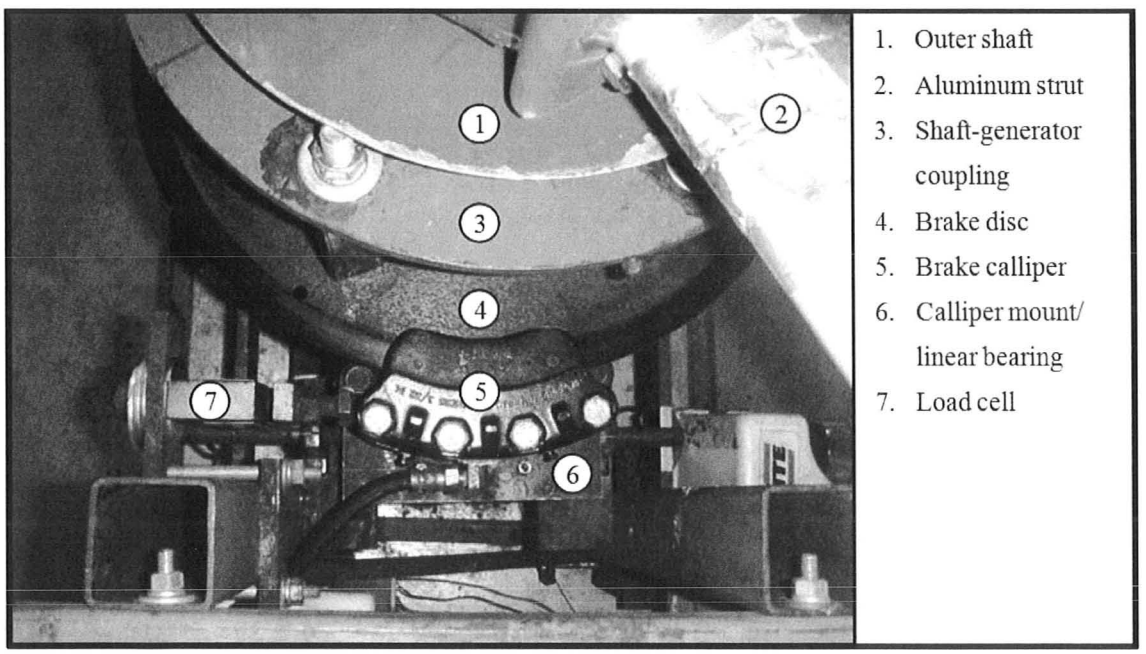

Figure 4-3: Top down view of the braking system used on the experimental turbine. Power output measured using a floating brake caliper which pushes up against a load cell when a load is applied (turbine rotates clockwise).

While it is not impossible under certain favourable conditions for a VAWT to self start (i.e.: when exposed to a sufficient headwind and no load is applied), in practise this occurrence is rare, thus an external energy source is required to bring the turbine up to a sufficiently high rpm in order for it to sustain rotation. This setup employs a Leeson C182-D17FK3 DC electric motor with a drive belt and a gear reduction ratio of 5.0 between the generator and the drive pulley, to apply the necessary starting torque. The drive pulley is fitted with a freewheel mechanism so as to allow the turbine to spin independently of the DC motor when it reaches its operating rpm. Flow velocity measurements in the wind tunnel experiments were taken with a R.M. Young 05305AQ propeller anemometer.

4.2 Turbine Control System

The prototype VAWT is controlled by a proportional controller that sends a pulse width modulated signal based on the difference between the actual and desired turbine rpm (Bravo *et al.*, 2007). The turbine rotational frequency and the load cell voltage signals are fed into an 8 channel data acquisition board (NI-DAQ 6015) which is controlled by a laptop computer running the National Instruments LABVIEW software. It was necessary to modify the brake actuator and bypass the factory installed electronic circuitry which was built into the unit in order to send the appropriate DC voltage to the hydraulic pump motor and PWM signal to the solenoid valve. Also, the solenoid valve was carefully over-bored in order to lower the minimum operating pressure from >700

kPa to approximately 70 kPa. A much finer control over the applied braking pressure was achievable as a result of the modifications, which resulted in the minimization of large turbine rpm fluctuations by approximately an order of magnitude from ± 5 rpm to ± 0.5 rpm when the brake was applied and released.

The proximity sensor was moved from sensing the bolts at the top of the generator to sensing equally spaced bolts at the base of the generator. The lower amplitudes of vibration at the base of the generator resulted in fewer dropped rpm signals, and a much more reliable rpm reading, which minimized the times the brake was actuated inadvertently and resulting in rpm control to within ± 0.1 rpm.

4.3 Turbine Performance

The original prototype VAWT, before any modifications were made, was wind tunnel tested on a tower that was centered in the National Research Council (NRC) 9m x 9m wind tunnel facility. In order to develop a series of base case performance curves, uniform, steady, low turbulence flows were applied ranging from the cut-in flow velocity of 6m/s up to 16m/s in 2m/s increments. The results from those tests are shown in Figure 4-4 and while the specific details may be found in Bravo *et al.* (2007).

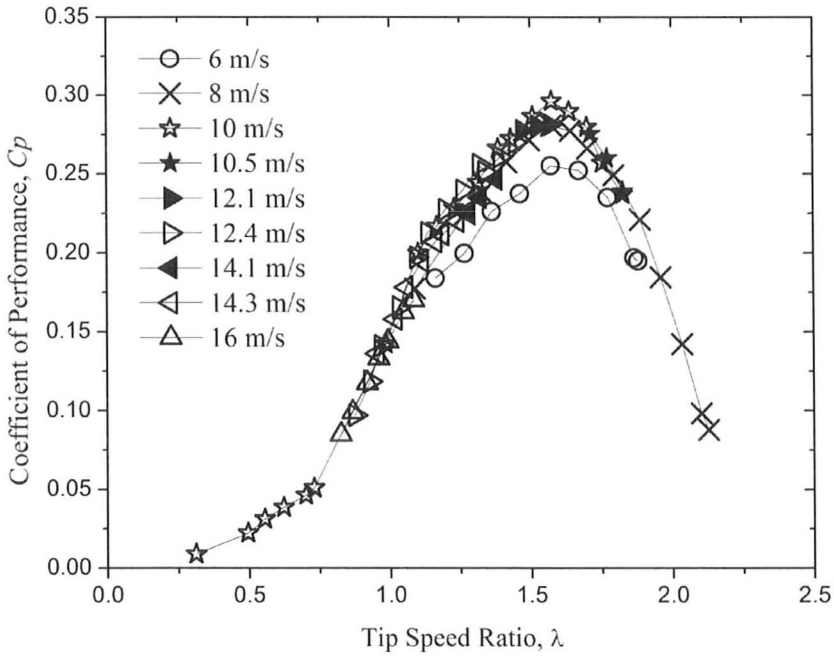

Figure 4-4: Non-dimensional performance curves obtained from wind tunnel tests at NRC in Ottawa, ON (Bravo *et al.*, 2007).

The power curves shown in Figure 4-4 appear to collapse relatively well with the exception of the 6m/s case. This deviation of this curve at lower flow velocities was attributed to the lower Reynolds number experienced by the turbine blades which has an adverse effect on performance. Peak turbine operation was observed when $\lambda = 1.6$ and $Cp = 0.29$.

A second series of base case tests were performed in the 8m wide by 5m high open air wind tunnel at the University of Waterloo Fire Research Laboratory. The facility consists of a large steel barn-like structure, with a bank of 6 fans which move the flow in the open air wind tunnel. The 74.6kW vane axial fans (Howden-Buffalo Model 78-26

Series 1000) are 1.98m in diameter, and are arranged in an array of 3 wide by 2 high in the plenum chamber. The plenum chamber is approximately 8m long by 8m wide by 6m high, and contains two flow settling screens located approximately 3.6m from the outlet of the fans. Flow straightening ducts are located at the exit of the plenum. The turbine centre was centered at 8m from the plenum exit. Results from flow measurement studies at this facility show a 5m x 8m area with relatively uniform flow (± 1m/s) in the location where the turbine was tested (Weisinger, 2004). The tests were performed with flow velocities ranging between 5m/s to 11m/s in 1m/s increments. The base case performance curves are shown in Figure 4-5. In these tests, the turbine struts were replaced with the square tube streamlined struts, the turbine was mounted to a short pedestal such that the bottom of the blades were 0.75m above the ground, and a larger instrument frame was installed.

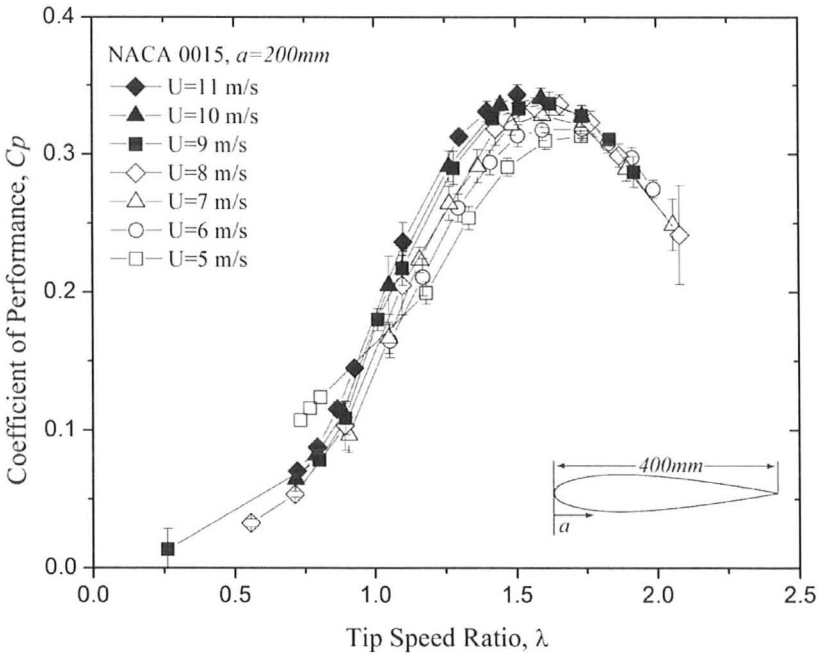

Figure 4-5: Non-dimensional performance curves of base case tests at the University of Waterloo open air wind tunnel, Waterloo, ON.

The results shown in Figure 4-5 compare relatively well with the results from Bravo *et al.* (2007). The power curves tend to collapse above 8m/s due to the decreasing dependence on Reynolds number. For the 10m/s case, $Cp_{max} \approx 0.34$ at a TSR close to 1.6, and is consistent with the findings of Bravo *et al.* (2007). A detailed examination of these results is presented in §5.1.

4.4 Blade Pitch and Mount Point Offset

As a result, initial investigations into blade preset pitch and mount point offset were performed in a simple fashion to determine the viability of a more in depth investigation. Blade preset pitch tests were performed by sandwiching washers between

the blade mount point and the strut until the desired angle was achieved. Mount point offset tests were initially evaluated through the use of two sets of NACA 0015 blades; one set with the mount location at $a = 200mm$ and the other set with mounts at $a = 150mm$. After significant performance changes were realized between the different pitch and offset cases, adjustable blade preset pitch and offset adapters were fabricated to perform a complete study.

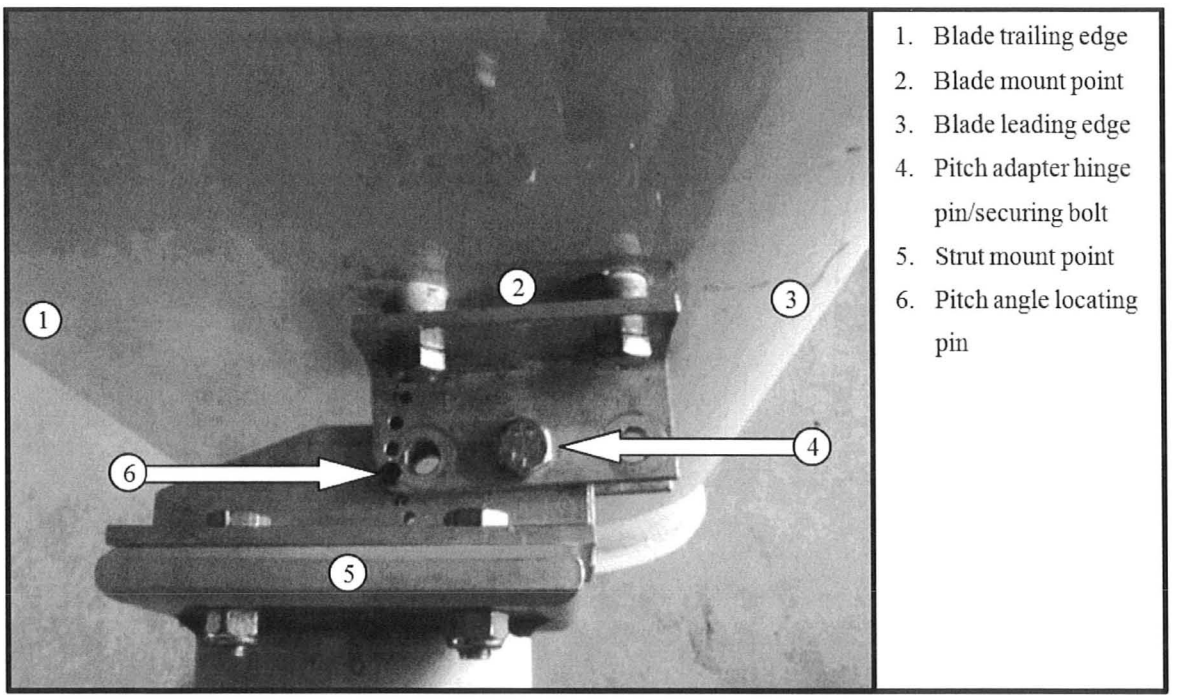

Figure 4-6: Top view of blade preset pitch adapter set to $\beta = -3°$ (toe-out).

The blade preset pitch adapter was designed and manufactured out of extruded aluminum angle in order to minimize weight and to obtain a high tolerance fit. A hinge was created by sandwiching two back-to-back pieces of angle that are attached to the blade mount between two others attached to the strut. A 0.5 in. bolt was used as the hinge

pivot pin. In order to set a range of desired angles, a series of holes were drilled at a common radius from the hinge pivot pin, through which a smaller locating pin could be placed, effectively fixing the assembly at a predetermined angle. The angle locating holes were drilled in such a manner so as to attain the widest range of possible angles centered about 0° in 3° increments. Using these adapters, angles ranging from $-21° \leq \beta \leq 18°$ were achievable; however, in practice only angles ranging between $-9° \leq \beta \leq 6°$ were required (refer to Figure 2-4). Figure 4-6 shows the adapter with the locating pin in place. Due to the fluctuating loads imposed on the airfoil during operation, the hinge pins and the locating pins were tightened down to eliminate any vibration within the hinge mechanism.

Blade mount point offset was accomplished in a similar manner to blade pitch, by means of aluminum angle adapters. Longer lengths of aluminum angle were mounted to the strut mount point providing locations along which the blade could be attached. The blade side adapter was designed to fit both the hinge strut side adapter as well as the offset strut side adapter so as to avoid duplication. Two locating holes were used to orient the blade at the appropriate blade offset location, and the same bolts that were used for the hinge pin were employed for the offset mount as shown in Figure 4-7.

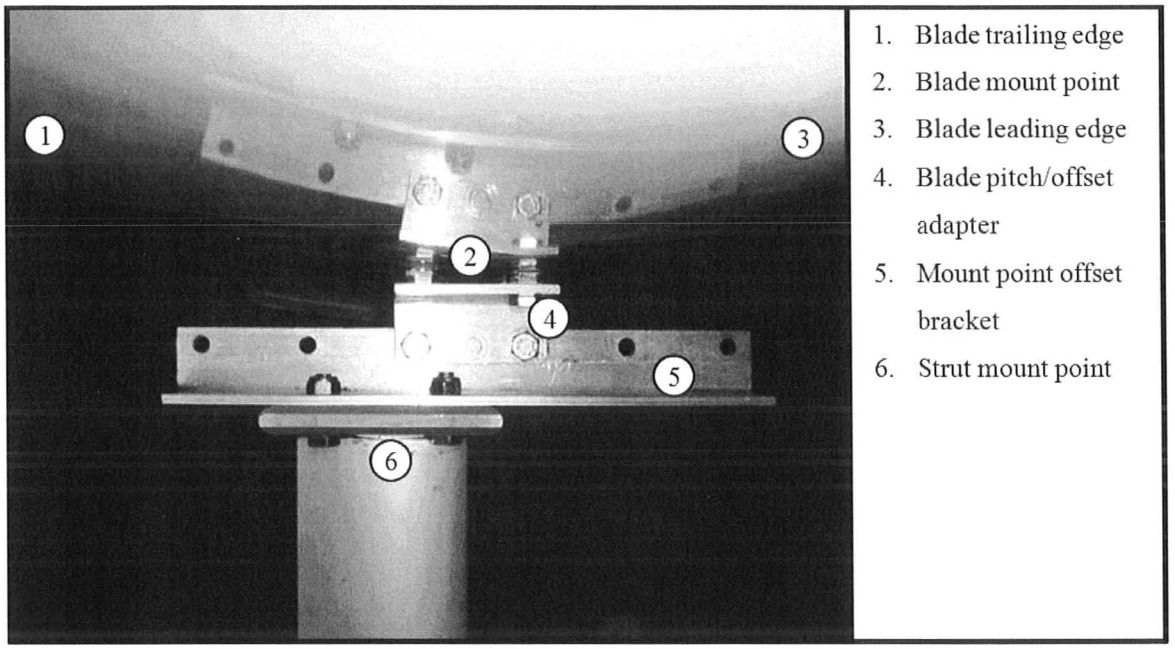

Figure 4-7: Top view of blade mount point offset adapter mounted at a = 200mm (mid-chord).

4.5 Wind Turbine Losses

Different turbine shafts were required due to variations in the span-wise spacing between adjacent mount-points on the different blade profiles resulting from manufacturing constraints. To compare performance changes brought about by changes in blade profile and configuration, the frictional losses of the different shafts and the aerodynamic drag due to the struts had to be accounted for and included in the comparisons. This was accomplished by measuring the electrical power required by a DC motor to maintain the different shaft-strut combinations at typical operating speeds. The DC motor efficiency was calculated by using a simple prony brake setup and was then included in the power loss calculations. A detailed explanation of this procedure is

outlined in Appendix A. The loss curves for the two shafts that were used in the preliminary wind tunnel tests are shown in Figure 4-8:

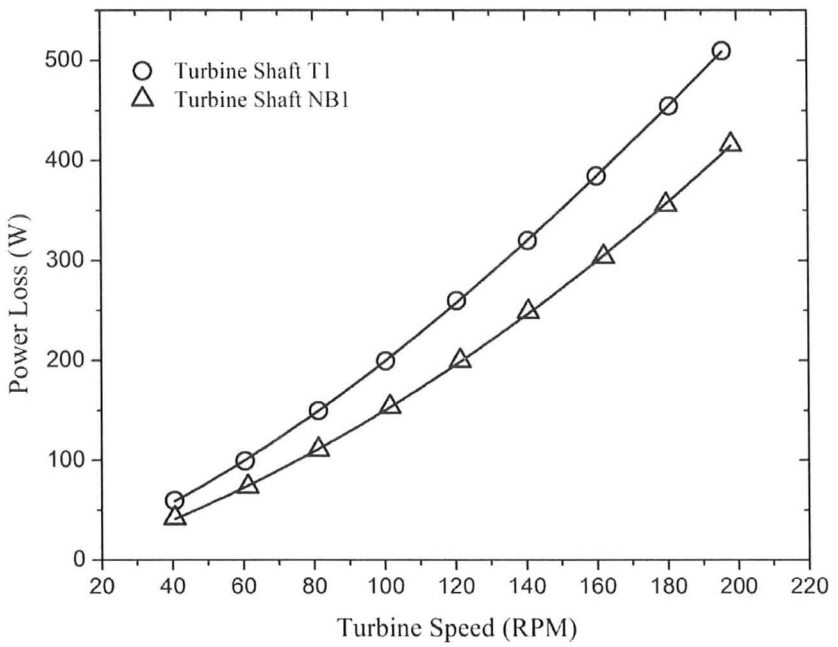

Figure 4-8: Power loss curves for the turbines tested during the preliminary wind tunnel tests. Both frictional bearing losses, as well as aerodynamic losses due to struts are included.

CHAPTER 5: RESULTS AND DISCUSSION

Experiments were conducted in an open-air wind tunnel to determine the effects blade preset pitch and mount point offset have on turbine performance. Two dimensional computational fluid dynamics simulations were also performed. Tufts were used to visualize the reversed flow along the inboard surface of the airfoil and the flow visualization data is presented for both experimental and CFD tests. The wind turbine was tested at the wind tunnel on two separate occasions, and although the results from both tests were very similar, the detailed summaries of the results obtained are presented in two separate sections in this chapter for clarity. The CFD simulations were performed concurrently with the second visit to the wind tunnel and are therefore presented with the second set of experimental results.

5.1 PRELIMINARY WIND TUNNEL TESTING

Several turbine blade configurations with varying degrees of blade preset pitch and mount point offset were tested. A complete non-dimensional performance curve was generated for the mid-mount NACA 0015 blades in order to have a base case with which to compare the remaining test data. A second, less refined performance curve was created with the forward-mount NACA 0015 blades. A third performance curve was created with the forward-mount NACA 0021 blades. These forward-mount configurations (NACA 0015 and NACA 0021) were then tested with preset pitch angles of +/- 3.9° and +/- 7.8°.A summary of the VAWT configurations is given in Table 5-1.

Test	Blade Profile	Turbine Shaft Designation	Mount Location (measured from L.E.), *a* [mm]	Preset Pitch Angle, β [deg]
1	NACA 0015	T1	200	+0°
2	NACA 0015	NB1	145	+0°
3	NACA 0021	NB1	150	+0°
4	NACA 0015	NB1	145	+3.9°
5	NACA 0015	NB1	145	+7.8°
6	NACA 0015	NB1	145	-3.9°
7	NACA 0015	NB1	145	-7.8°
8	NACA 0021	NB1	150	+3.9°
9	NACA 0021	NB1	150	+7.8°
10	NACA 0021	NB1	150	-3.9°
11	NACA 0021	NB1	150	-7.8°

Table 5-1: VAWT Test and configuration matrix for preliminary wind tunnel testing.

The results for the Test 1 blade configuration are shown in Figure 5-1. The data is plotted using non-dimensional power curves. Error bars are included on the averaged data points in Figure 5-1 indicating one standard deviation. For clarity, lines connecting the data points have been included, and the error bars have been omitted on subsequent plots since they are rarely larger than the symbol size. The results show that the turbine operates at relatively low TSR. Both South and Rangi (1972), and Klimas and Worstell (1981), had low solidity turbines whose Cp_{max} occur at $\lambda \approx 5.5$. The high solidity and blockage ratio of this turbine results in peak operation at $\lambda \approx 1.6$. It can be seen that as the wind velocity increases, the peak Cp also tends to increase slightly. At higher wind velocities, Cp_{max} tends to be converging on $Cp \approx 0.34$, and the power curves are observed to collapse above 8m/s due to the decreasing dependence on Reynolds number. For the 10m/s case, $Cp_{max} \approx 0.34$ at $\lambda = 1.6$. As mentioned in §4.3, these results exhibit the same

trends observed by Bravo *et al.* (2007). The magnitudes of the performance curves differ slightly due to compensation for frictional and aerodynamic losses which was included in Figure 5-1. For comparison with other cases, only the 10m/s cases are considered.

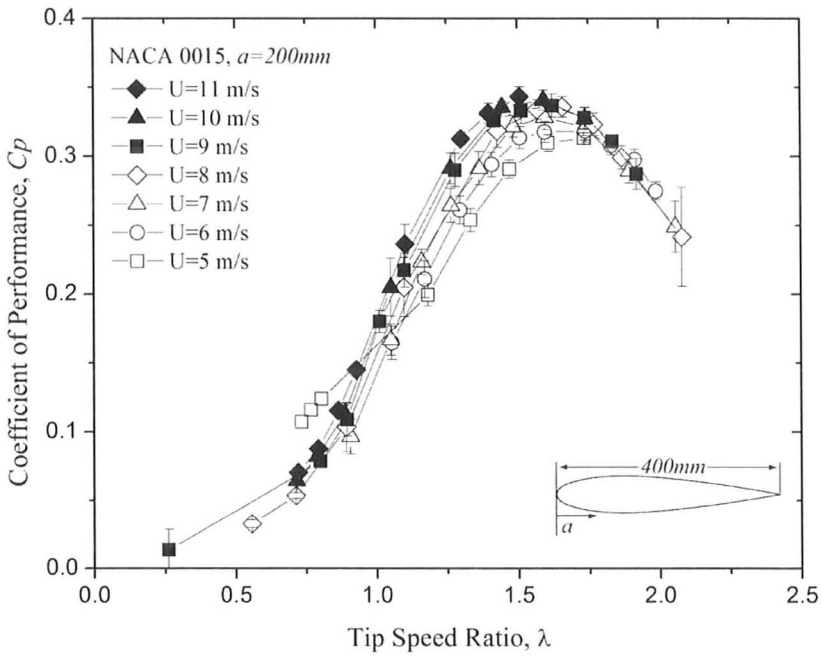

Figure 5-1: Non-dimensional performance curves for Test 1, NACA 0015 profile, mid-mount ($a = 200mm$), $\beta = 0°$, over a range of wind velocities.

Figure 5-2 illustrates the results of Tests 1 and 2. For these tests, the effect of strut mounting positions on turbine performance was investigated. A noticeable drop in performance ($\Delta Cp_{max} = 0.086$) was seen with the NACA 0015 blades with a forward mounting position ($a = 145mm$). This forward shift of mount-point corresponds to an effective toe in pitch change of 2.5° ($\beta = +2.5°$). These results are consistent with the findings of Paraschivoiu (2002).

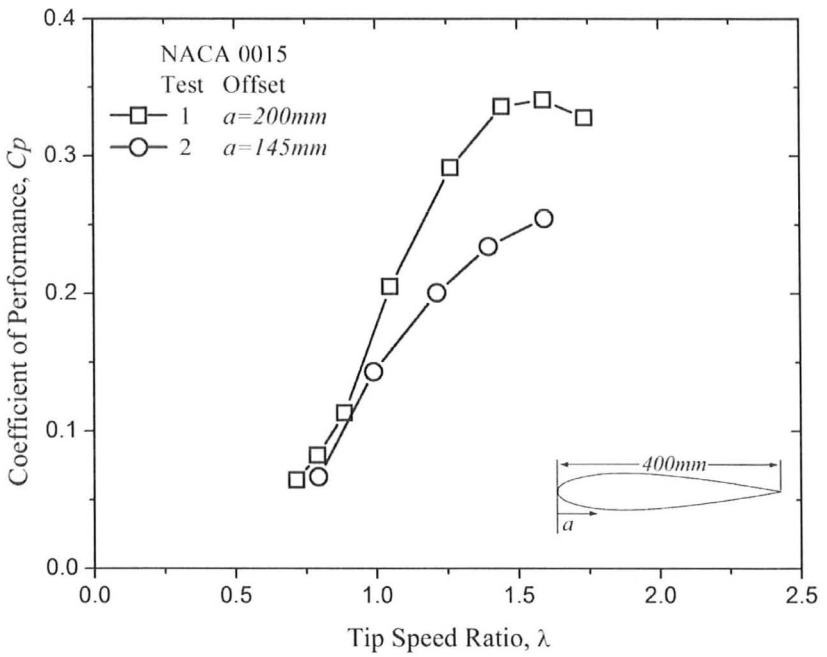

Figure 5-2: Non-dimensional performance curves for NACA 0015 profile, comparing effect of blade mount-point location offset for $U_\infty = 10m/s$.

The results of the preset pitch tests are presented in Figure 5-3 and Figure 5-5. Tests 2, and 4 through 7, demonstrate the effects of preset pitch on the NACA 0015 profile. It is emphasized that the strut mounting location on the blade for these tests has the inherent effect of 2.5° toe-in at mid-chord. The tests were performed with additional preset pitch angles of ±3.9° and ±7.8°, resulting in pitch angles of β = *-5.3°, -1.4°, +2.5°, +6.4°, +10.3°* when referenced to a mid-chord mount location.

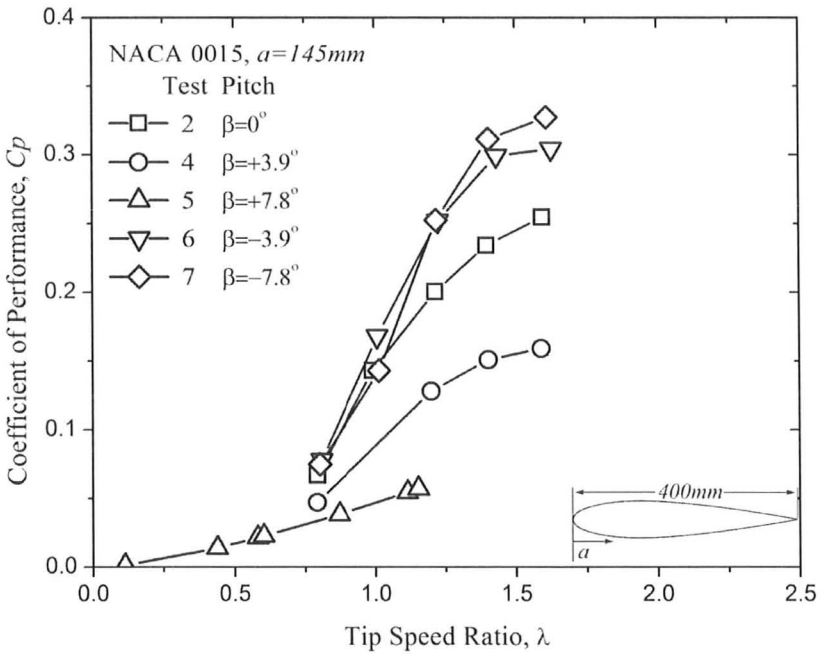

Figure 5-3: Non-dimensional performance curves illustrating the effects of varying preset pitch, β, on NACA 0015 ($a = 145mm$) blades for $U_\infty = 10m/s$.

Positive values of preset pitch ($\beta > 0$, toe-in) are not desirable from a performance standpoint. In Figure 5-3, Cp_{max} dropped by approximately 37% for $\beta = +3.9°$, compared to the zero pitch case. For $\beta = +7.8°$ the turbine was unable to overcome frictional and aerodynamic losses or generate any useful torque. A gain in Cp_{max} of 20% was observed for Test 6, corresponding to a preset pitch $\beta = -3.9°$ (toe-out). When the pitch was changed to $\beta = -7.8°$ in Test 7, an additional increase of 9% was observed, resulting in $Cp_{max} = 0.33$. At lower values of TSR, there was no noticeable advantage with the $\beta = -7.8°$ case, and the performance curve crosses beneath the curve for $\beta = -3.9°$. For all preset pitch values, the TSR corresponding with the peak Cp was observed to remain constant with the peak TSR for $\beta = 0°$.

It should be noted that in the case of Test 6 (NACA 0015, $\beta = -3.9°$, $a = 145mm$), the performance curve approaches the performance of Test 1 (NACA 0015, $\beta = 0°$, $a = 200mm$). This is largely due to the toe-out preset negating the effect of the forward mount location which was applying an effective toe-in offset. This is an important result, as it may be desirable from a structural or vibration point of view to have the mount location towards the leading edge of the airfoil where it is closer to the centre of pressure; but from a performance point of view, a toe-out preset must be applied in order to prevent lower power outputs. This general behaviour of performance gains with toe-out presets and performance losses with toe-in presets is similar to that in the literature for lower solidity VAWTs that was presented earlier.

It is also emphasized that the mount-point location was varied for these tests, and a preset pitch was then applied to minimize any performance losses due to this mount-point offset. For blades with different mount-point locations, the zero-wind AOA for the leading and trailing edges (as well as over the entire chord of the blade) may be determined from Equation (2-7). Another point of interest is the cross-over of toe-out performance curves at lower values of TSR. The performance curve becomes sharper with increased toe-out preset, resulting in gains in the Cp_{max}, but has inferior performance at lower values of TSR as a consequence.

The results from Tests 2 and 3 are presented in Figure 5-4. For these tests, NACA 0015 and NACA 0021 profiles were compared. The NACA 0021 profile resulted in $Cp_{max} = 0.29$ at $\lambda = 1.45$. This peak TSR ($\lambda = 1.45$) is lower than for the NACA 0015 profile (λ

= *1.6*). It is hypothesized that this is due to more gentle dynamic stall performance. Overall, turbine performance is improved over a broad range of TSR for the NACA 0021 profile.

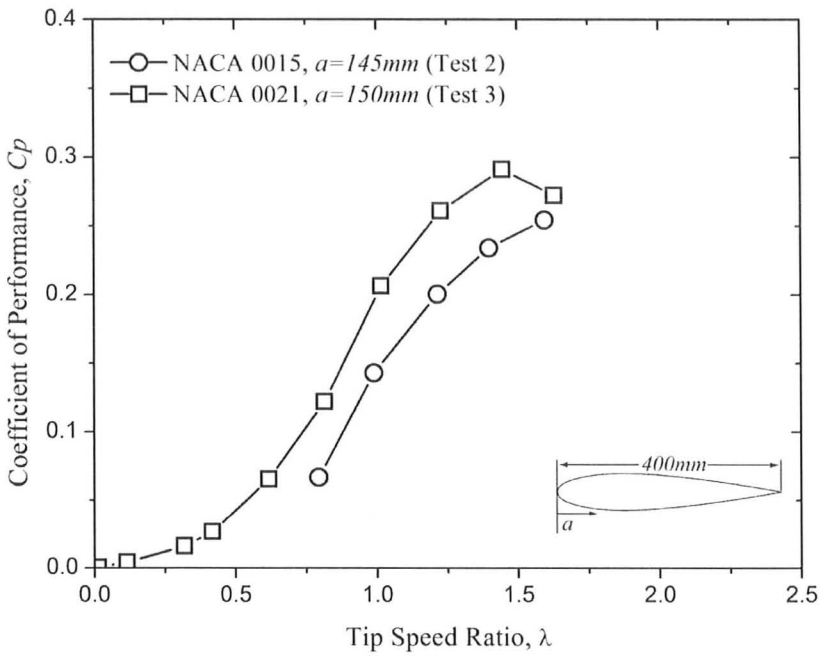

Figure 5-4: Non-dimensional performance curves comparing the effect of NACA 0015 and NACA 0021 blade profiles on performance for U_∞ = *10m/s*.

Tests 3, and 8 through 11, demonstrate the effects of added preset pitch on the NACA 0021 profile in Figure 5-5. The mount location for this profile results in an inherent 2.3° toe-in, to which the same additional presets of ±3.9° and ±7.8° were added.

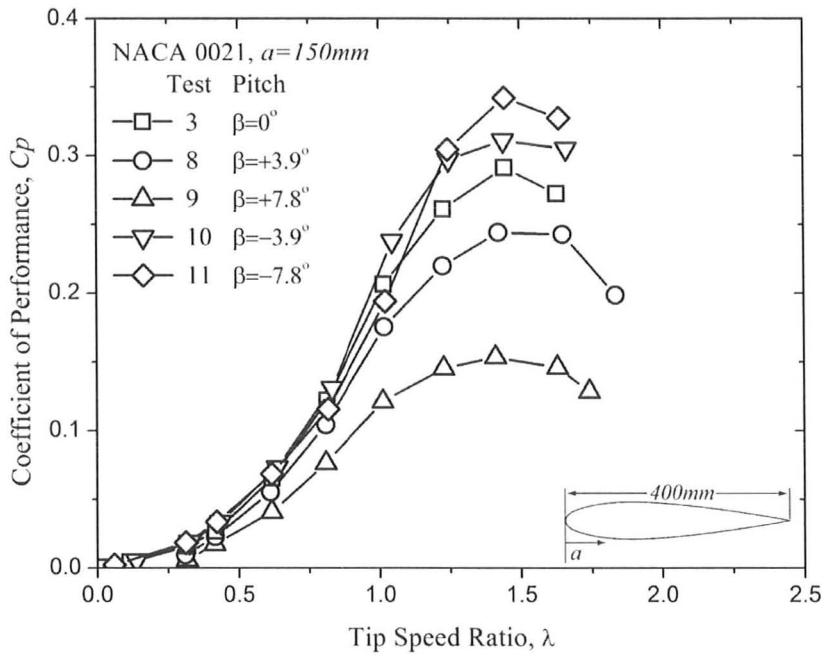

Figure 5-5: Effects Non-dimensional performance curves illustrating the effects of varying preset pitch, β, on NACA 0021 ($a = 150mm$) blades for $U_\infty = 10m/s$.

For the NACA 0021 airfoils, Figure 5-5 shows Cp_{max} dropped by 16% and 47% for $\beta = +3.9°$ and $\beta = +7.8°$, respectively, relative to the zero pitch case. For $\beta = +7.8°$ the turbine was still able to operate, in contrast with the same pitch NACA 0015 case seen in Figure 6. Gains in Cp_{max} of 7% and 18% were observed for $\beta = -3.9°$ and $\beta = -7.8°$. As with the NACA 0015 profile, gains in Cp for the NACA 0021 profile with $\beta = -7.8°$ over the $\beta = -3.9°$ are only present in the peak TSR range. The trend of the $\beta = -7.8°$ curve to cross beneath the $\beta = -3.9°$ curve is also apparent. As with the NACA 0015 profile, for the NACA 0021 toe-in preset pitch, the TSR corresponding with the peak Cp was observed to remain constant with the peak TSR for $\beta = 0°$.

The performance increases observed arising from mount points which are further from the leading edge as well as with toe-out preset pitch configurations are thought to be

related due to their geometric similarity. A more extensive series of wind tunnel tests was performed to better observe the relationship between blade preset pitch and mount point offset.

5.2 Extensive Wind Tunnel Testing

A second extensive series of experimental tests was performed to gain a more thorough understanding between the relationship of blade preset pitch and blade mount point offset. Although the tests were similar to those outlined in §5.1, they were performed using longer aluminum struts and specially fabricated blade pitch and offset adapters. As a result of these changes, the turbine radius was increased from 1.25m to 1.475m, resulting in an increase in projected area of 1.35m^2. The resulting solidity was decreased from $\sigma = 0.48$ to $\sigma = 0.41$, and therefore comparisons between the two results are limited to the observed trends.

For simplicity, the important parameters of the tests have been summarized in Table 5-2. The tests were performed first using the NACA 0015 blade profile, and subsequently the same tests were repeated with the slightly thicker NACA 0021 blade profile. All wind tunnel tests were performed at a constant flow velocity of 10m/s. This velocity was chosen because it has been shown in §5.1that Reynolds number effects on airfoil performance are not significant above 8m/s for a similar turbine configuration in this wind tunnel, and to facilitate comparisons between existing wind tunnel experiments. For the sake of simplicity and to avoid repetition, the tests involving the NACA 0015 airfoil will be denoted with the 'a' suffix, while those involving the NACA 0021 airfoil

will be labelled with a 'b' suffix (i.e.: Test 1a involves NACA 0015, Test 1b is identical in all respects but the profile is NACA 0021).

Test #	Blade Profile	Turbine Shaft Designation	Mount Location (Measured from L.E.), a [mm]	Preset Pitch Angle, β [deg]	Equivalent Blade Pitch, β [deg]	Comment
1	a) NACA 0015 b)NACA 0021	NB1	200	5.99	-	Toe IN
2	a) NACA 0015 b)NACA 0021	NB1	200	3.00	-	Toe IN
3	a) NACA 0015 b)NACA 0021	NB1	200	0.00	-	Neutral
4	a) NACA 0015 b)NACA 0021	NB1	200	-3.00	-	Toe OUT
5	a) NACA 0015 b)NACA 0021	NB1	200	-6.01	-	Toe OUT
6	a) NACA 0015 b)NACA 0021	NB1	200	-9.02	-	Toe OUT
7	a) NACA 0015 b)NACA 0021	NB1	200	-12.04	-	Toe OUT
8	a) NACA 0015 b)NACA 0021	NB1	53	0.00	5.69	Toe IN
9	a) NACA 0015 b)NACA 0021	NB1	126.5	0.00	2.85	Toe IN
10	a) NACA 0015 b)NACA 0021	NB1	273.5	0.00	-2.85	Toe OUT
11	a) NACA 0015 b)NACA 0021	NB1	347	0.00	-5.69	Toe OUT

Table 5-2: VAWT test summary and configuration matrix for secondary wind tunnel tests.

It is worth mentioning that the slight variations in the preset pitch angle (and the equivalent blade pitch), β, in Table 5-2 are attributed to design constraints limited by the offset nature of the mount points on the blades. These slight variations from the nearest

integer values of β were not observed to cause significant performance changes and thus were deemed suitable for comparison.

All performance data is presented in the form of non-dimensional power curves of coefficient of performance (Cp) versus the blade tip speed ratio (λ). The results for Tests 1a – 7a are shown in Figure 5-6. For these tests, the effects of varying the blade preset pitch were investigated. The high solidity and blockage ratio of this turbine results in peak operation at $\lambda \approx 1.6$. The $\beta = 0°$ curve is taken as the base case (for the NACA 0015 profile) with which the other NACA 0015 profile curves are compared. Peak Cp for this curve is $Cp_{max} = 0.27$ at $\lambda = 1.63$. Turbine performance was observed to decrease as the amount of toe-in pitch is increased (as β becomes more positive) due to early onset stall resulting from the increased AOA encountered by the blades on the upwind blade pass combined with less thrust generated on the downwind pass ensuing from lower AOA. The blade thrust force as a function of blade orbital position is presented later and discussed in the context of the numerical results.

As the blade preset pitch is changed to the toe-out configuration ($\beta < 0°$), performance increases are observed for the $\beta = -3°$ and $\beta = -6°$ cases. For the $\beta = -3°$ case, performance peaked at $Cp_{max} = 0.30$, and a slight increase to $Cp_{max} = 0.32$ was observed for the $\beta = -6°$ case. The ideal tip speed ratio appeared relatively consistent at $\lambda = 1.63$. Further increases in toe-out preset pitch result in sharp performance decreases. For example, when the preset pitch was changed by an additional 3° to $\beta = -9°$, the peak Cp occurred at $Cp_{max} = 0.26$, which is close to the zero preset pitch base case. A further

increase in toe-out preset pitch to $\beta = -12°$ is accompanied by a performance decrease of 86% at $Cp_{max} = 0.04$. For this blade profile, varying the blade preset pitch resulted in performance increases of up to 18% relative to the zero preset pitch case.

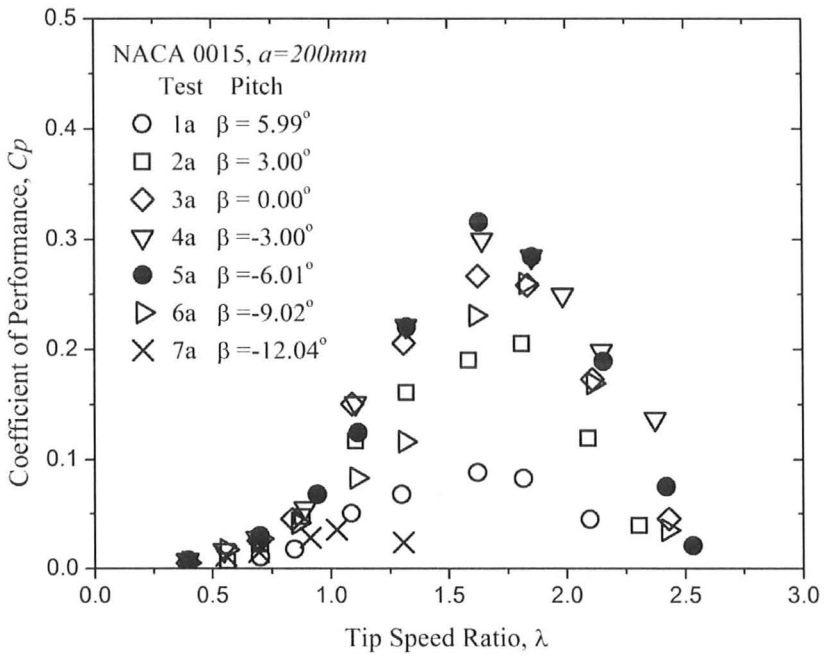

Figure 5-6: Non-dimensional performance curves for Tests 1a – 7a illustrating the effect of varying the preset pitch, β, on a VAWT with NACA 0015 blades for U_∞ = *10m/s*.

The effects of blade mount point offset (Tests 3a and 8a-11a) can be observed in Figure 5-7. As the blade mount point was shifted towards the trailing edge ($a > 200mm$), increases in Cp were observed. The curves for $a = 273.5mm$ and $a = 347mm$ both peak at $Cp_{max} = 0.29$ and $\lambda = 1.60$, a 9.5% increase to the mid-mount (zero offset; $a = 200mm$) case. Peak Cp for both the $a = 126.5mm$ and the $a = 53mm$ case decreased to $Cp_{max} = 0.21$ and $Cp_{max} = 0.13$ respectively. The tip speed ratio at Cp_{max} did not change appreciably and remained at $\lambda \approx 1.60$.

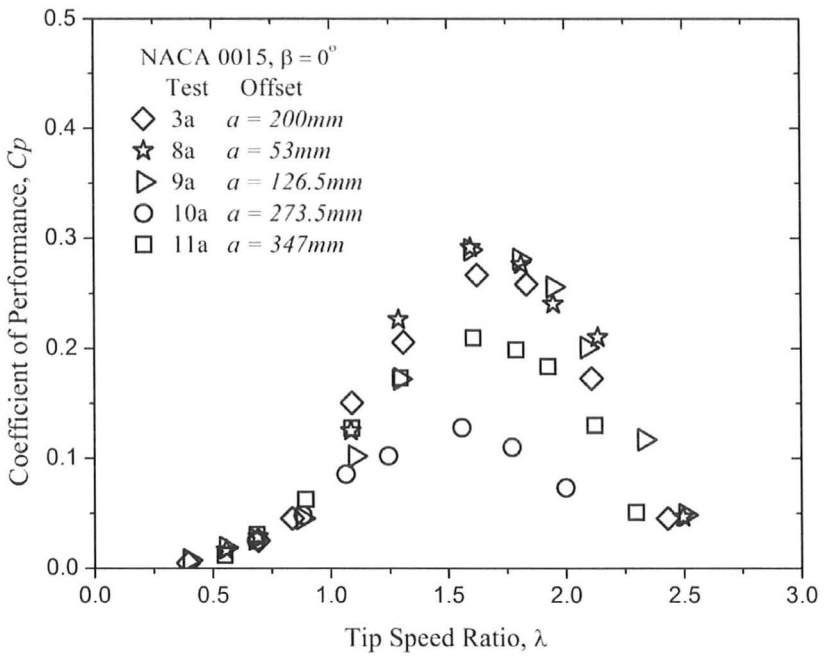

Figure 5-7: Non-dimensional performance curves for Tests 3a and 8a – lla illustrating the effect of varying the mount point offset, *a*, on a VAWT with NACA 0015 blades for U_∞ = *10m/s*.

As the blade pitch, β, is adjusted to a toe-out condition, the non-dimensional performance curve is observed to become narrower, and has a sharper peak, than the toe-in configurations. Similar behaviour can be seen when the blade offset is adjusted to yield an effective toe-out blade pitch configuration. A slight crossover of the $\beta = -6°$, $a = 347mm$ and $a = 273.5mm$ can be seen in the vicinity of $\lambda = 1.10$.

An overlay of Figure 5-6 and Figure 5-7 is shown in Figure 5-8 below. The base case ($\beta = 0°$, $a = 200mm$) curve has been omitted for clarity and to avoid repetition. The performance curves of the preset pitch cases, illustrated by the outlined markers are in very good agreement with the solid markers representing the blade mount point offset tests having the equivalent blade pitch. The effects of blade preset pitch and blade mount

point offset are also in good agreement to the trends seen in §5.1. Although the turbine radius is slightly increased when the blade mount point is offset to yield a certain equivalent blade pitch, the results for this turbine show that for a *c/r = 400mm/1475mm = 0.27* turbine, a 5% max increase in radius does not affect non-dimensionalized turbine performance significantly compared with the performance increase resulting from the introduction of an effective blade pitch.

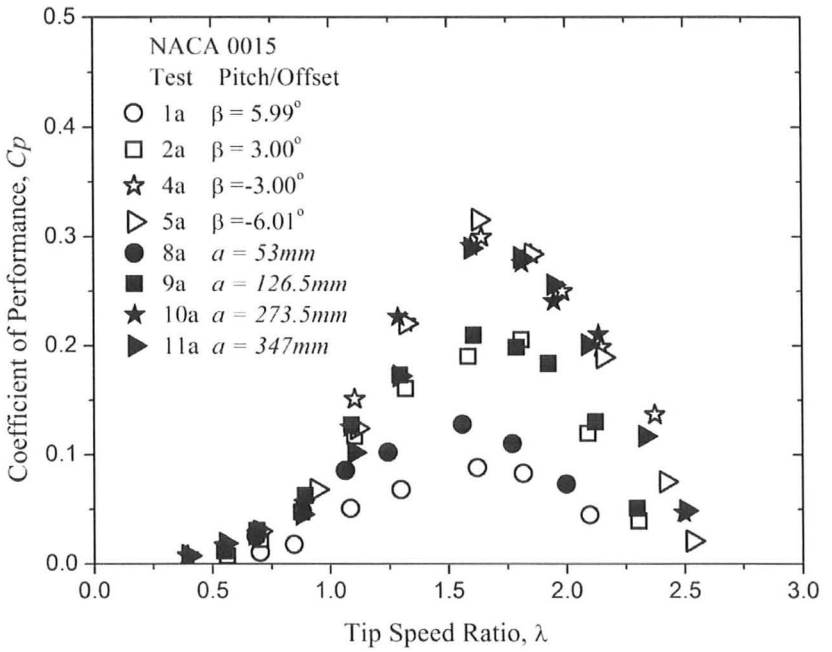

Figure 5-8: Non-dimensional performance curves for Tests 1a, 2a, 4a, 5a, and 8a – 11a comparing the effects of varying the mount point offset, *a*, with blade preset pitch, *β*, on a VAWT with NACA 0015 blades for U_∞ = *10m/s*.

An analogous series of tests were performed using the NACA 0021 profile. The results of tests 1b, 2b, 4b, 5b, and 8b – 11b are shown in Figure 5-9. Only the figure illustrating the relative behaviour of blade pitch and blade offset is shown as the individual trends of both curves mimic those presented for the NACA 0015 case.

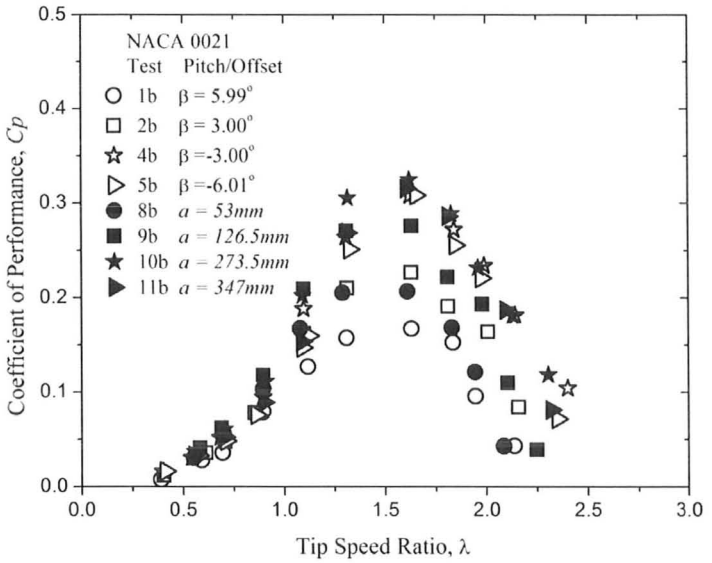

Figure 5-9: Non-dimensional performance curves for Tests 1b, 2b, 4b, 5b, and 8b – 11b, comparing the effects of varying the mount point offset, *a*, with blade preset pitch, *β*, on a VAWT with NACA 0021 blades for U_∞ = *10m/s*.

For all configurations, the peak tip speed ratio (λ at Cp_{max}) appeared to be fairly constant at $\lambda \approx 1.62$. For the blade preset pitch tests (Tests 1b, 2b, 4b, 5b) maximum performance was observed with the toe-out ($\beta = -3°$, $\beta = -6°$) cases at which peak power occurred at $Cp_{max} = 0.31$. Toe-in performance resulted in decreased peak performance for $\beta = 3°$, $\beta = 6°$ with peak Cp occurring at $Cp = 0.23$ and $Cp = 0.17$ respectively. The mount point offset tests showed peak performance when $a = 347mm$ and $a = 273.5mm$ ($Cp = 0.32$ and $Cp_{max} = 0.33$). Blade offsets corresponding to a toe-in configuration ($a = 126.5mm$ and $a = 53mm$) yielded lower peak performance coefficients ($Cp = 0.28$ and $Cp = 0.21$ respectively). Reasonably good agreement is seen between the toe-out blade pitch and corresponding blade mount point offset tests. Also apparent is the narrowing behaviour of the Cp curve as toe-out pitch is applied, and the broadening of the curve as

toe-in pitch is applied – behaviour that was exhibited with the NACA 0015 blade profile, and was observed previously in §5.1.

Flow visualization techniques were also used to qualitatively investigate the flow patterns on the blade surface. A video camera was mounted to the turbine shaft facing radially outwards at a turbine blade. Bi-coloured Mylar tufts approximately 4cm long by

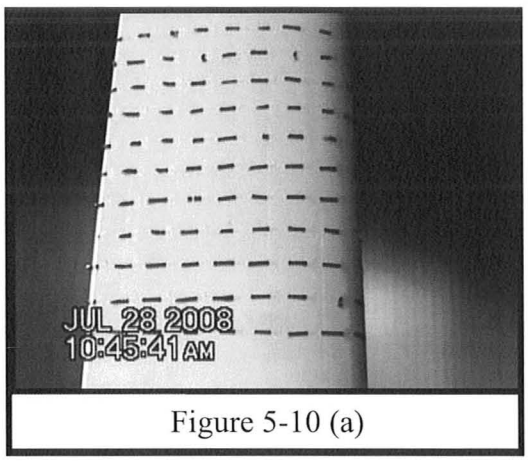

Figure 5-10 (a)

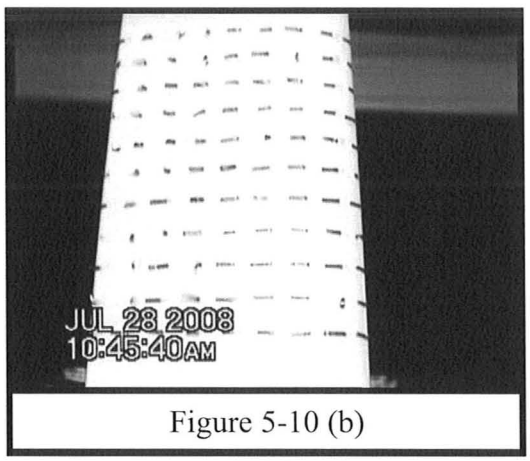

Figure 5-10 (b)

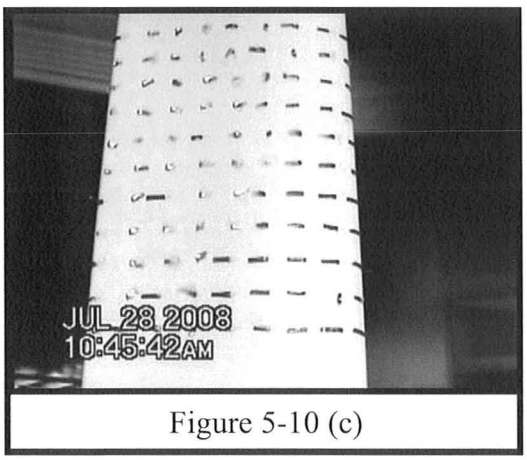

Figure 5-10 (c)

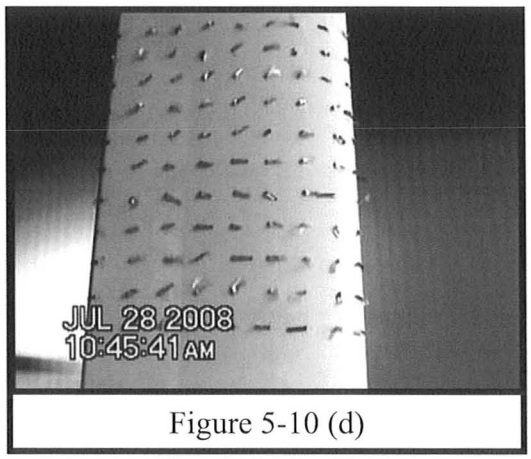

Figure 5-10 (d)

Figure 5-10: Select examples of distinct stall regions identified in the analysis tuft flow visualization on the inner surface of a VAWT blade. Blade trailing edge appears on the left while the leading edge appears on the right in each image. Subfigure (a) no reversed flow, (b) reversed flow at trailing edge, (c) reversed flow across half chord, (d) fully reversed flow over entire lower blade surface.

0.5cm wide were arranged in a square array on the inner surface of the turbine blade, in plain view of the camera. The tuft array extends 0.5m above the strut to view the regions of the blade where the flow is affected by the strut. Observations indicated that the top half of the array was unaffected by the flows around the strut.

The camera field of view was adjusted to focus on the array of tufts on the blade surface, as well as to include some background features of the wind tunnel which were used to determine the orbital location of the turbine blade. The extremely light and flexible nature of the Mylar tufts allowed very fast tuft response times when subjected to rapid fluctuations in airflow direction. The bi-coloured nature of the tufts results in easy identification of zones of reversed flow over the blade. When the flow over the inner blade surface is from the leading to the trailing edge, the red side of the tufts is shown; however, when the flow is reversed, the silvered underside of the tufts is seen.

Frame by frame visual analysis of the tuft video footage as the blade travels around its orbital path, an example of which is shown in Figure 5-10, yields the orbital locations at which the airfoil experiences various stages of stall. Four distinct categories of stall on the inner blade surface have been identified in order to consistently classify the tuft behaviour from case to case. The first is 'no stall', and occurs when the red surface is observed on all tufts in the array (Figure 5-10.a). The next stage is incipient stall, which was interpreted as occurring when reversed flow is observed along the trailing edge of the blade (Figure 5-10.b). When reversed flow was observed over half of the blade chord, it was considered 'half-blade stall' (Figure 5-10.c). Similarly, when the flow was reversed

over the majority of the chord, the condition was described as being fully stalled (Figure 5-10.d).

The camera used for the flow visualization was a standard commercially available digital video camcorder which has a standard frame rate of 30 frames per second. At peak tip speed ratio ($\lambda = 1.6$), the turbine angular velocity was approximately $10.85\ rad/s$, which results in 17 video frames taken every revolution. There was little revolution-to-revolution variation seen in the video footage, but to ensure that any revolution-to-revolution variation was indeed negligible, the video footage that was analyzed was subsequently averaged. The pie graph in Figure 5-11 represents a plan view of the turbine and provides a graphical representation of the various stall zones encountered by a single blade as it travels along its trajectory while it is operating at peak power ($\beta = 0°, \lambda = 1.6$). As the turbine blade approaches $\theta = 90°$ the angles of attack experienced by the blade are increased and incipient trailing edge stall was observed, indicated by the yellow region in the graph. As the blade continues along its trajectory, the angles of attack continue to increase until the blade becomes fully stalled. When the blade passes $\theta = 180°$, assuming there are no wakes or vortices in its vicinity, the angles of attack become progressively smaller, and the flow is no longer reversed. From the pie chart, it is apparent that the blade is experiencing stall behaviour for nearly half of its entire revolution. Minimizing the size of the overall stalled region is important to improving turbine efficiency.

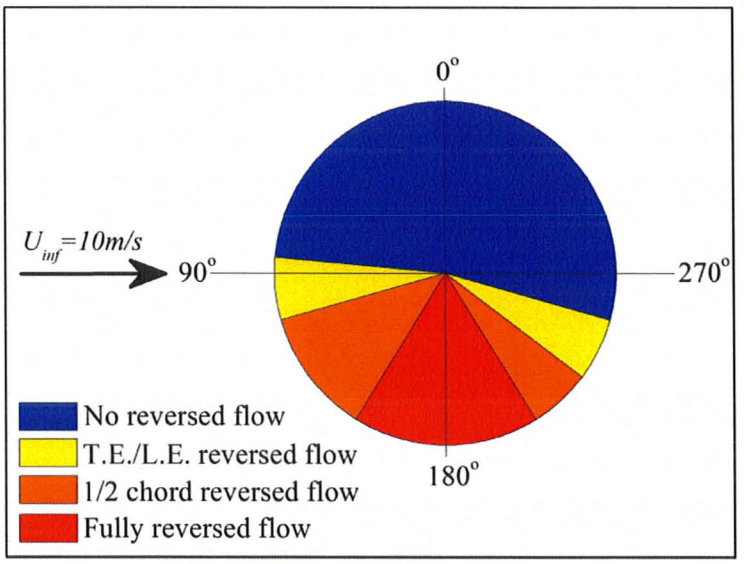

Figure 5-11: Stall behaviour for a single NACA 0015 blade ($\beta = 0°$, $\lambda = 1.6$) displayed on a plan view of the turbine blade orbit. As illustrated, the nominal wind is from the left at 10m/s.

In order to facilitate comparison between various tip speed ratios at different preset pitch cases, the pie charts are 'unwrapped' and displayed as stacked bar graphs. Figure 5-12 shows the qualitative results obtained from the tuft visualization for a single NACA 0015 blade at pitch values $\beta = 0°, -3°, -6°, -9°$ and tip speed ratios $\lambda = 1.1, 1.3,$ and 1.6. In a manner analogous to that of the pie chart, the colours on the bar graph represent the degree of stall experienced by the turbine blade. The zero degree orbital position datum is taken when the blade is heading directly upstream into the oncoming wind as shown in Figure 5-11.

Observation of the stall behaviour of the $\beta = 0°$ case in Figure 5-12 indicates that at lower than peak tip speed ratios ($\lambda < 1.6$), the blade experiences significant amounts of reversed flow over the course of its orbit. As the tip speed ratio is increased, the angles of attack experienced by the blade at any given θ will be decreased, resulting in a delay in

the onset of each separate stall regime. This phenomenon is present for all tested blade preset pitch angles.

The effects of varying the blade preset pitch for a constant tip speed ratio are described below. For $\lambda = 1.1$, as the blade preset pitch is decreased (more toe-out is added), the overall range of the stalled blade decreases from 180° when $\beta = 0°$ to 170° when $\beta = -6°$. As toe-out is increased further, performance is seen to decrease with the blade experiencing stall over 180° of its orbit when $\beta = -9°$. The range over which the blade appears to be fully stalled when $\lambda = 1.1$ is also observed to decrease with increase in toe-out, from 110° when $\beta = 0°$ down to 85° with the peak toe-out value of $\beta = -6°$. Increasing the toe-out preset further to $\beta = -9°$ is accompanied by a performance drop, indicated by the 115° range of full stall.

A similar trend is seen for the $\lambda = 1.3$ case. As the blade pitch is varied from $\beta = 0°$ to $\beta = -3°$, -6°, and -9°, the blade is fully stalled for $\theta = 70°$, 80°, 65°, and 85° respectively. It should be noted that for this case, the full stall behaviour commences at a later position, and finished at a later position compared with the $\lambda = 1.1$ case. Likewise, for the $\lambda = 1.6$ case, the blade appears to be fully stalled for $\theta = 60°$, 60°, 40°, and 60° for the previously mentioned preset pitch angles, and once again, the full stall regime commences and ends at higher values of θ.

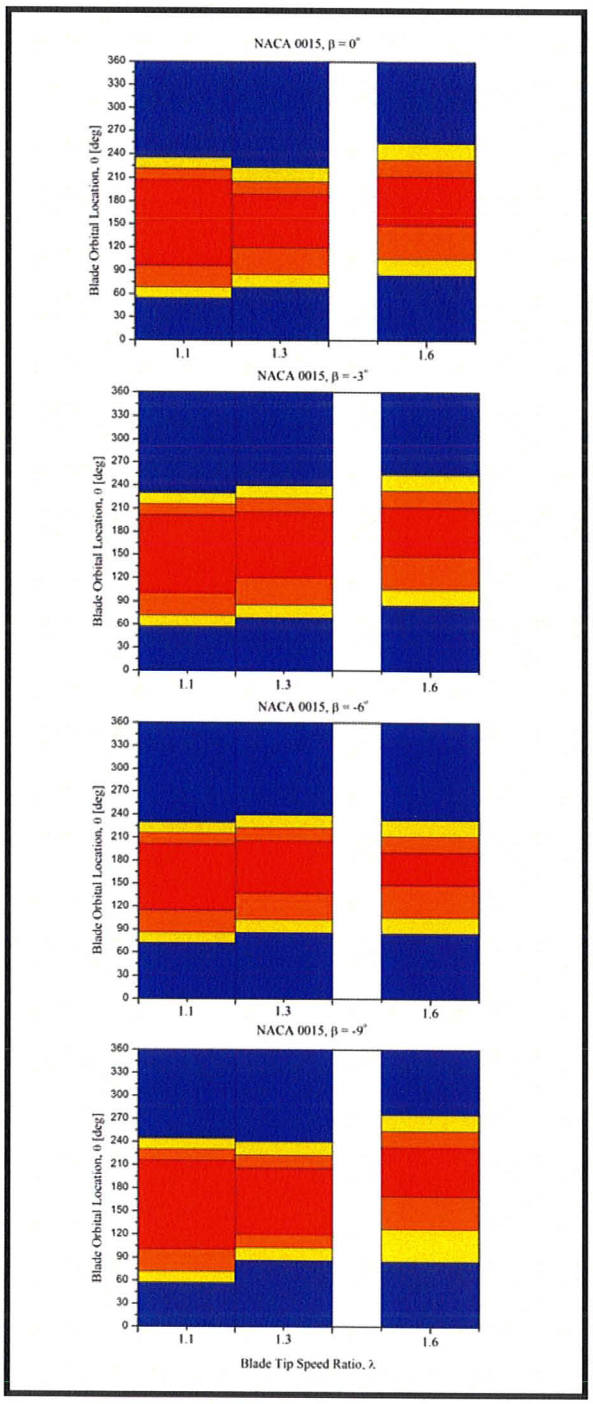

Figure 5-12: Stall plots for a one of three NACA 0015 airfoils for various blade preset pitch angles, β, and for three different tip speed ratios, λ (Cp_{max} occurs at $\lambda=1.6$). Flow velocity was constant at 10m/s. Colour scheme representing the regions of reversed flow is as defined in Figure 5-11.

It is emphasized that changing the blade preset pitch does not have the same effect on performance as changing the blade tip speed ratio. For a given blade tip speed ratio, an increase in blade toe-out (a decrease in β) towards the optimal preset pitch will result in a diminished region of full stall. It is hypothesized that the blade is experiencing more desirable nominal angles of attack on both the upwind and downwind passes, resulting in preferable dynamic stall behaviour. On the other hand, for a given blade preset pitch, an increase in blade tip speed ratio will result in two changes.

In a manner analogous to increasing toe-out pitch, an increase in tip speed ratio will also result in the blade experiencing full stall for a shorter duration. In addition, this decreased full stall duration is accompanied by a shift of the full stall regime to higher values of θ. These are important results because they qualitatively demonstrate the relative importance of keeping the turbine operating at its peak tip speed ratio (in this case peak TSR occurs at $\lambda = 1.6$), and illustrate the diminishing full stall regime resulting from presetting the blade pitch in an optimal toe-out configuration. Reducing the size of the full stall regime at peak tip speed ratio by applying toe-out preset pitch may also help in reducing the high vibration amplitudes that result from blades which stall suddenly and remain stalled for longer durations.

5.3 CFD Simulation Results

The 2-D CFD model presented in §3.3 was used to investigate the effects of blade pitch and blade mount point offset. A complete in-depth description of this model may be found in McLaren *et al.* (2009).

All the simulations were performed using a 13.45m/s inlet wind velocity with an inlet turbulence intensity of 5%. Because the experimental results showed significant performance decreases for toe-in configurations, simulations were only performed on the toe-out blade preset pitch tests for β = 0°, -3°, -6°, and -9° (Tests 3a – 6a) involving the NACA 0015 profile (refer to Table 5-2). Each preset pitch configuration was simulated at λ = 1.1, 1.3, 1.6, 1.8, 2.1, 2.3, and 2.5. Supplementary simulations were performed on the β = -6° case at λ = 1.95, 2.7, and 2.9, resulting in 31 simulations in total. The results from these simulations are presented on a non-dimensional performance curve in Figure 5-13.

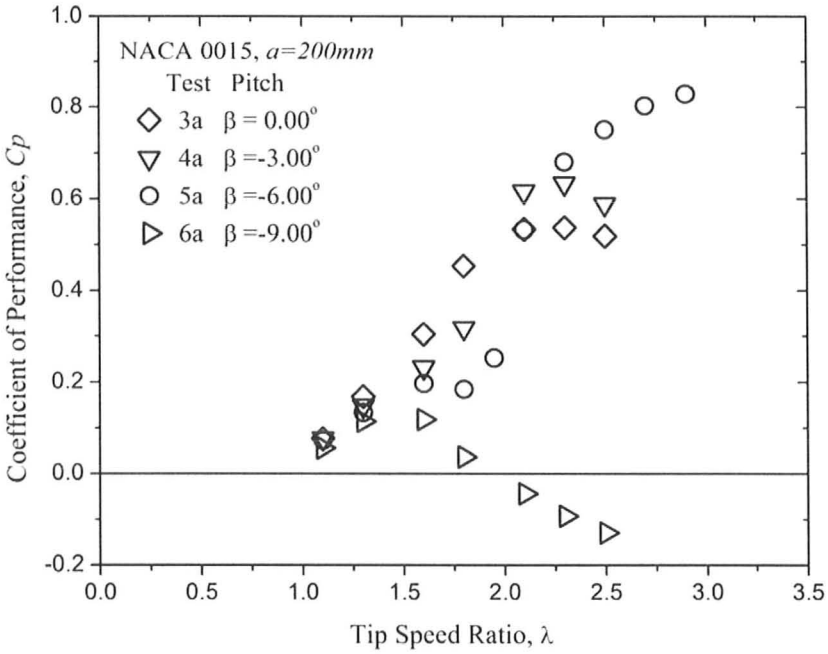

Figure 5-13: Non-dimensional CFD performance curves for Tests 3a – 6a comparing the effects of varying the blade preset pitch, β, on a VAWT with NACA 0015 blades for $U_\infty = 13.45m/s$.

In a similar manner to the experimental results, the $\beta = 0°$ case is taken as the base case with which the others are compared. As seen in Figure 5-13, the $\beta = 0°$ case peaks at $\lambda = 2.3$, and exhibits a similarly shaped power curve compared with the experimental results. The big difference between these results and the experimental ones is that the peak Cp is nearly doubled and occurs at a much higher λ. This behaviour was expected based on the 2-D CFD results of Howell *et al.* (2009) and McLaren *et al.* (2009). The two dimensional approximation does not allow for flow above and below the turbine, resulting in a semi-ducted condition. As a result, the free-stream velocity, U_∞, entering the simulated turbine is higher than for a free-air turbine resulting in higher Cp values occurring at higher λ. Therefore, the 2-D flow simulation and its corresponding

free-air case do not occur at the same tip speed ratio; rather, the equivalent 2-D simulation occurs at a higher tip speed ratio.

When the blade pitch is changed to $\beta = -3°$, a toe-out configuration, a 17% increase in the performance is seen compared with the zero preset pitch case. This peak also occurs at $\lambda = 2.3$. The phenomenon of a narrowing and higher peaking Cp curve as toe-out preset pitch was increased was mentioned in §5.1, and was also observed in the experimental wind tunnel results. As the toe-out angle was increased beyond $\beta = -3°$ to $\beta = -6°$, a dip in the performance curve is observed at $\lambda = 1.8$. The high peak of the Cp is not seen even at $\lambda = 2.7$. When $\beta = -9°$, Cp_{max} is only 23% of Cp_{max} for $\beta = 0°$, while λ_{peak} occurs at 70% of λ_{peak} when $\beta = 0°$. The behaviour exhibited is similar to that of the higher toe-out experimental results ($\beta < -6°$). The flows observed in the CFD simulations are quite complex. The vortex shedding during the upwind blade pass observed by McLaren *et al.* (2009) was seen at the lower tip speed ratios (λ <1.8). A weaker vortex appeared to be shed as the blade completes its orbit towards the end of the downwind pass, also consistent with the findings of McLaren *et al.* (2009).

Plots indicating regions of reversed flow on the inner blade surface were created from the CFD results in a similar manner to those of the experimental results. Snapshots showing the flow patterns local to the blade were made in the rotating reference frame at 10° intervals as it travelled along its orbital path. Figure 5-14 illustrates the four distinct stall regions which were defined in Figure 5-10 in order to allow for comparison with the experimental results. The upper surface of the airfoil in the plan view snapshots (Figure

5-14) is the airfoil outer surface, while the lower surface of the airfoil is the inner surface. Akin to tuft analysis presented earlier for the experimental results, the snapshots were analyzed individually and each was assigned a stall designation from which a stall plot was subsequently created.

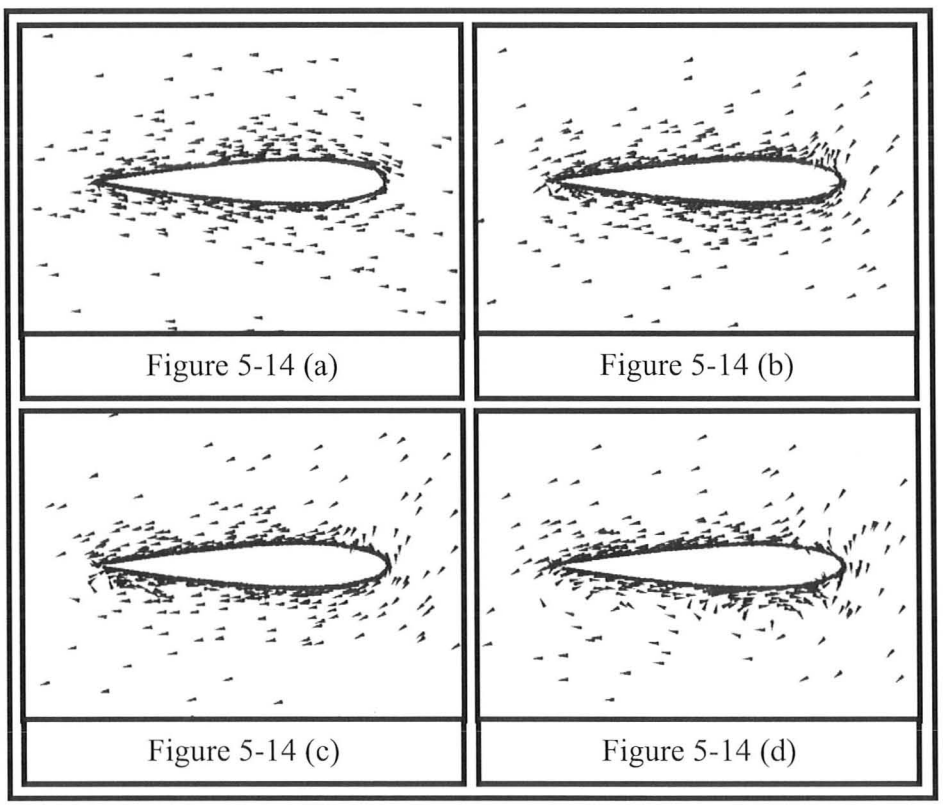

Figure 5-14: Select examples of distinct stall regions identified in the analysis of CFD flow visualization on the inner (lower) surface of a VAWT blade. Subfigure (a) no reversed flow, (b) reversed flow at trailing edge, (c) reversed flow across half chord, (d) fully reversed flow over entire lower blade surface.

The stall plots that were generated from the two dimensional CFD simulations are presented in the following figures. Figure 5-15 illustrates the effect of increasing blade speed ratio on the inner stall behaviour of a NACA 0015 airfoil mounted at mid-chord (a = 200mm), with $\beta = 0°$ preset pitch.

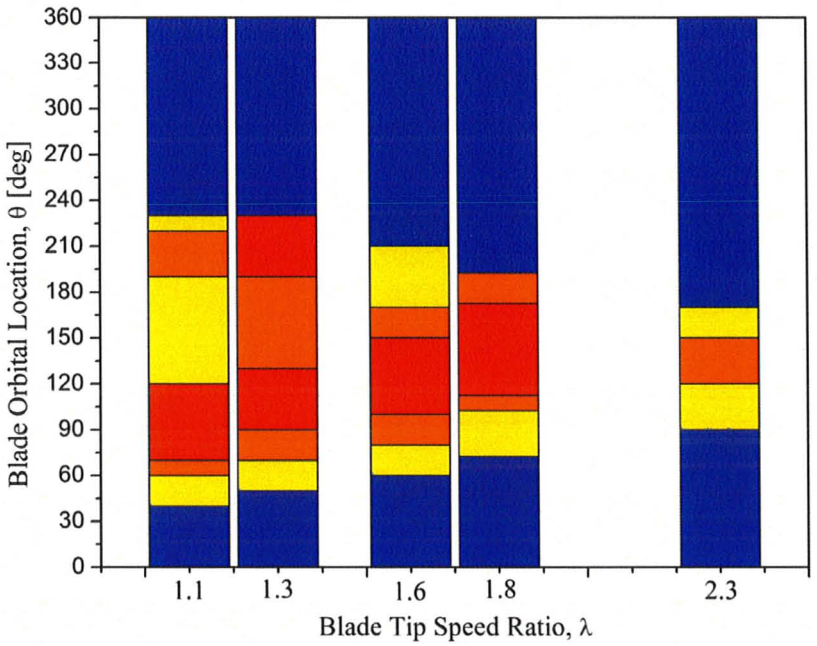

Figure 5-15: CFD Stall plot showing the effects of increasing tip speed ratio on stall behaviour for the inner blade surface of a NACA 0015 blade ($a = 200mm$, $\beta = 0°$). Colour scheme representing the regions of reversed flow is as defined in Figure 5-11.

As the blade tip speed ratio is increased, the onset of incipient trailing edge stall is retarded to a later orbital position (see Figure 5-15). Increasing the blade tip speed ratio also appears to reduce the total duration that the inner blade surface experiences any reversed flow, which is consistent with the results obtained from the experimental tuft visualizations shown in Figure 5-12. Since it is difficult to quantify nominal angles of attack in a highly dynamic and complex flow, this phenomenon may be explained by modelling the blade as a single point and noting that as the tip speed ratio is increased, the theoretical angles of attack would be decreased on both the upwind and downwind blade passes. The Reynolds numbers local to the blade would also be higher, allowing the blade to experience higher angles of attack before experiencing reversed flow.

The differences exhibited between $\lambda = 1.1$ and $\lambda = 1.3$ may be attributed to blade-vortex interaction. Observations of the CFD simulations indicate that at lower tip speed ratios, a vortex is created on the upwind blade pass as the airfoil begins to experience reversed flow, is subsequently shed from the blade, and is then convected downstream at the local flow velocity; behaviour that is consistent with the findings of McLaren *et al.* (2009). Under low tip speed ratios, it is possible for the vortex to impinge on the same blade from which it was shed when it is on the downwind pass. This interaction disturbs the stall recovery of the airfoil, and the effects are apparent for the case of $\lambda = 1.3$ in Figure 5-15, where flow over half the blade chord remains reversed between $130° \leq \theta \leq 190°$ as the vortex approaches the airfoil, and reverts back to fully reversed for a short duration upon impingement. As the tip speed ratio is increased, the nominal angles of attack are reduced, until no vortices are shed during the upwind pass. It is hypothesized that this blade-vortex interaction behaviour was not seen in the experimental data presented in Figure 5-12 due to differences in equivalent tip speed ratio between the CFD and experimental results.

The effects of blade preset pitch on turbine performance at a given tip speed ratio is shown in both Figure 5-16 and Figure 5-17 for tip speed ratios $\lambda = 1.6$ and $\lambda = 2.3$ respectively. Although the numerical simulations cannot be used to determine absolute magnitudes and are used only to observe trends, CFD generated stall plots at tip speed ratios equal to the peak tip speed ratios of the experimental and CFD power curves are shown.

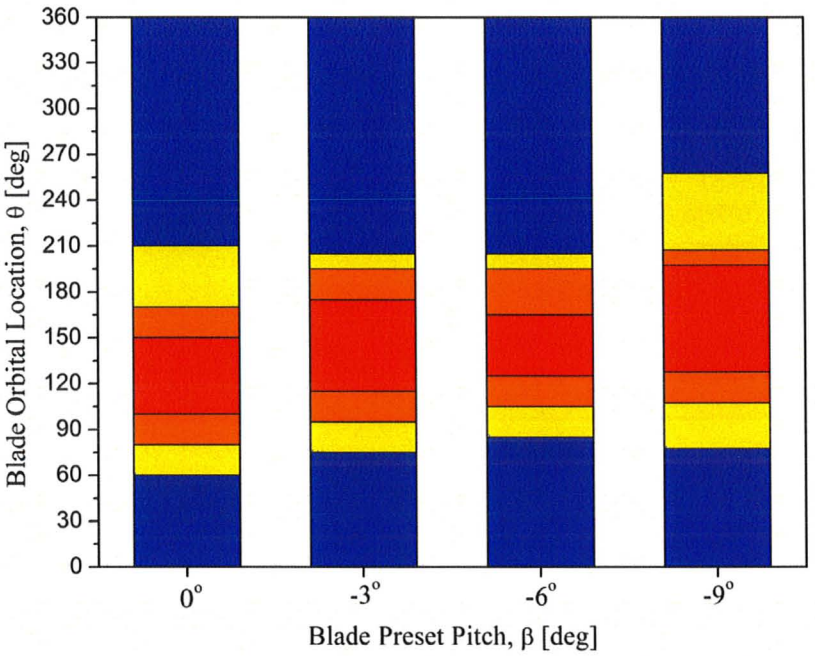

Figure 5-16: CFD Stall plot showing the effects of increasing toe-out blade pitch on stall behaviour for the inner blade surface of a NACA 0015 blade (a = 200mm, λ = 1.6). Colour scheme representing the regions of reversed flow is as defined in Figure 5-11.

Observation of the stall plot shown in Figure 5-16 shows incipient stall commencing at $\theta = 60°$ and all reverse flow ending at $\theta = 210°$ for the $\beta = 0°$ case, resulting in the inner blade surface being stalled over a total range of $\Delta\theta = 150°$ of the turbine's rotation, and the flow was observed to be fully reversed between $100° \leq \theta \leq 150°$. An increase of the toe-out preset pitch to $\beta = -3°$ is accompanied by a delay in the onset of trailing edge stall until $\theta = 75°$, and delaying full stall until $\theta = 115°$. The overall stall region exists between $75° \leq \theta \leq 205°$, that is $\Delta\theta = 130°$. This trend continues as the blade preset pitch is changed to $\beta = -6°$ (further increasing toe-out). The onset of stall is retarded to $\theta = 85°$ and the full stall regime exists between $125° \leq \theta \leq 165°$ with all reversed flow ceasing at $\theta = 205°$. Beyond the $\beta = -6°$ preset pitch threshold, an increase

in overall reversed flow on the inner surface of the airfoil was observed. Increasing the degree of toe-out to $\beta = -9°$ results in further decreases in AOA of the blade during the upwind pass and increases in AOA on the downwind pass.

While it is the general goal to lower upwind pass angles of attack to avoid reversed flow, while increasing power extracted on the downwind pass by increasing the amount of toe-out; when the optimal threshold is exceeded, relatively little lift on the upwind pass combined with augmented stall on the downwind pass will consequently result in a decrease in performance.

Similar trends are observed at the peak tip speed ratio of the CFD results ($\lambda = 2.3$), however due to the ducted nature of the 2-D simulation, the reversed flow on the inner surface of the blade does not approach the levels seen at lower tip speed ratios, and at the peak TSR in the experimental results shown in Figure 5-12. The greatest amount of reversed flow is present for $\Delta\theta = 30°$ when the reversed flow is encountered along at most half of the inner surface for $\beta = 0°$ (see Figure 5-17). Subsequent increases in toe-out to $\beta = -3°$ and $\beta = -6°$ are accompanied by decreasing stall regions which occur progressively later. As β decreased beyond the threshold value of $\beta = -6°$, the region of reversed flow begins to grow once again and turbine performance decreases. The power curves presented in Figure 5-13 illustrate this decrease in performance as the toe-out preset pitch is increased beyond $\beta = -6°$, and this result is also consistent with the power curves generated from wind tunnel experimentation shown in Figure 5-6. The delay

observed in the onset of reversed flow as tip speed ratio is increased is also seen in the experimental results of Figure 5-12.

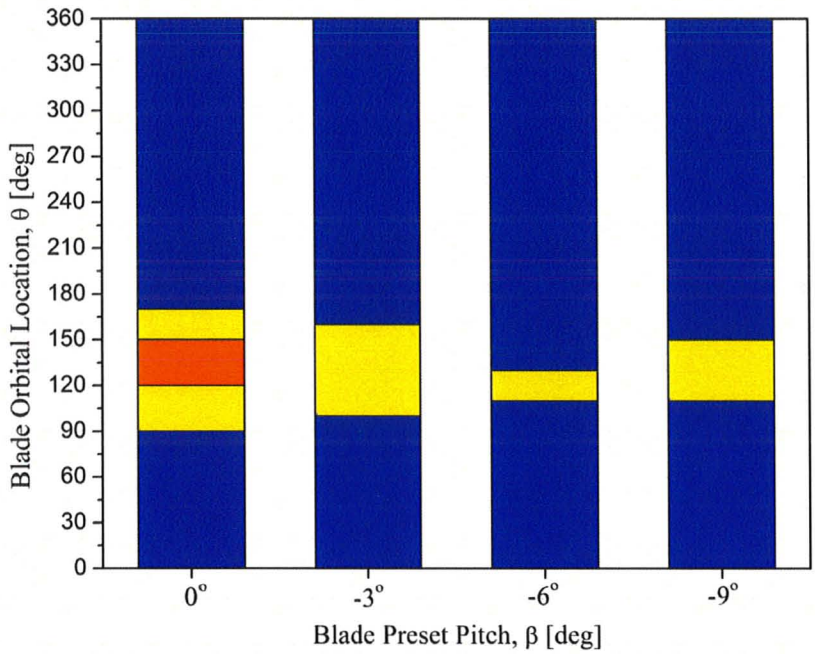

Figure 5-17: CFD Stall plot showing the effects of increasing toe-out blade pitch on stall behaviour for the inner blade surface of a NACA 0015 blade (a = 200mm, λ = 2.3). Colour scheme representing the regions of reversed flow is as defined in Figure 5-11.

The stall plots presented allow for qualitative comparison between the CFD and experimental results, however, in order to gain a more thorough understanding of pitch effects on performance, single blade torque curves are examined. These curves illustrate the torque generated by one of the three blades, T, as a function of turbine orbital position, θ. The torque data obtained from one of these curves is then integrated over the entire blade path and divided by turbine rotational frequency to yield overall single blade power per cycle. The integration of blade torque over the entire blade path means that the generated power is a balance between power extracted and dissipated on both the upwind

and downwind halves of the turbine. The curves are also used to compare predicted turbine stall characteristics with the qualitative tuft data presented earlier. Once again, the zero degree datum is defined as the location where the blade is travelling directly upstream to maintain consistency between the experimental and numerical results. Figure 5-18 shows the changes in single blade torque for various blade tip speed ratios at a constant blade preset pitch, β = -3°. This preset pitch case was chosen for analysis because the 2-D CFD simulations showed clear benefits of toe-out pitch. For this case, Cp_{max} occurs at λ = 2.3, as shown in Figure 5-13.

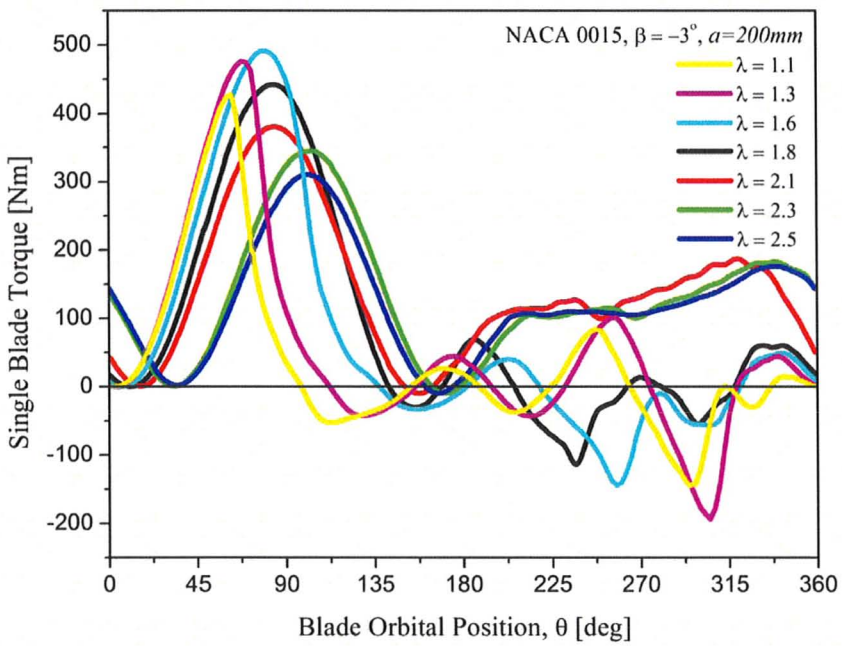

Figure 5-18: Single blade torque curves for Test 4a comparing the effects of varying the tip speed ratio on blade thrust (NACA 0015, β = -3°)

In theory, lower blade tip speed ratios will experience higher nominal angles of attack which will result in the blade stalling at earlier orbital positions (lower values of θ). For λ = 1.1, the parabolic shape of the torque curve on the upwind side is only

apparent up to the stall point which occurs relatively early on during the blade's orbit at $\theta = 60°$, after which the torque drops off rapidly indicative of a more sudden rather than gradual loss in lift. The blade appears to recover from the stall around $\theta = 110°$, but due to the relatively high angles of attack caused by lower nominal wind speeds, generates very little net positive torque during the entire downwind pass and proceeds to fluctuate between generating positive torque and negative torque several times during the downwind blade pass. In fact, very similar behaviour is seen for all blade tip speed ratios up to and including $\lambda = 1.8$. This behaviour is attributed to the blade-vortex interaction mentioned in the discussion of the stall plots of Figure 5-15. Observations of the flow field indicate the strongest blade-vortex interactions at the lowest tip speed ratios, which is consistent with the downwind pass torque fluctuations in Figure 5-18.

The increase in tip speed ratio however, results in lowering the nominal angles of attack on both the upwind and downwind passes, retarding the onset of blade stall to a higher θ, behaviour that was also observed in Figure 5-15. Interestingly, the peak of the torque curve on the upwind pass continues to increase in magnitude with increasing λ, up to $\lambda \leq 1.6$, after which it is observed to decrease. This may also be attributed to a decreasing range of angles of attack experienced by the airfoil as λ increases allowing the airfoil to generate positive torque longer, and given the absence of a sharp drop off (seen when $\lambda = 1.1$ and 1.3) after the peak may signify a reduction of the stall condition. As the tip speed ratio is increased further (towards optimal $\lambda = 2.3$), the peak thrust continues to decrease and occur at later orbital positions (θ), stall even more gently, and for $\lambda \geq 2.1$ the

production of significant net positive torque is seen over the majority of the downwind pass, a significant contributor to overall *Cp*.

From Figure 5-13 it is known that performance decreases slightly when $\lambda = 2.5$ compared to $\lambda = 2.3$, and this performance decrease can be attributed to the lower torque curve peak at $\theta = 100°$ given that the differences between the two curves are otherwise negligible. The torque curves are useful in identifying a range of acceptable operating blade speed ratios which generate negligible amounts of negative torque, indicating that while performance may not be at its highest; energy is not being periodically lost due to drag on the blade during the downwind pass, and vibrations resulting from this may be minimized.

The effects of varying the blade preset pitch are observed at the peak tip speed ratio, $\lambda = 2.3$, and only the effects of toe-out blade preset pitch ($\beta \leq 0°$) are shown in Figure 5-19 because it has been shown in the experimental results that toe-in preset pitch values ($\beta \geq 0°$) are detrimental to VAWT turbine performance.

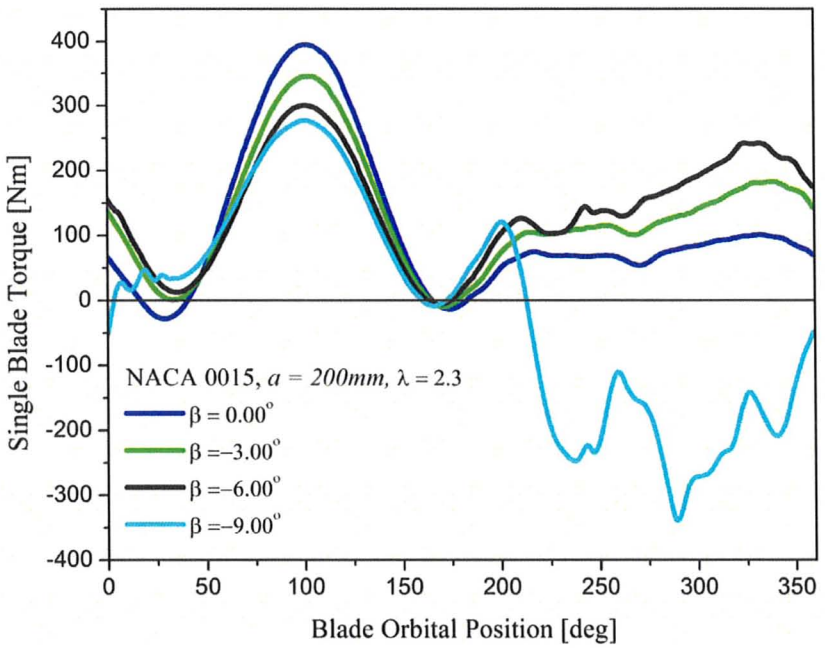

Figure 5-19: Single blade torque curves for Tests 3a – 6a comparing the effects of varying the blade preset pitch while holding the TSR constant (NACA 0015, $\lambda = 2.3$)

The zero preset pitch in this case yields the highest amount of torque on the upwind side, and while not resulting in any net negative torque, it does not generate comparatively much power on the downwind pass. As the toe-out preset pitch is increased (β is decreased), the nominal angles of attack on the upwind blade pass decrease while the angles of attack on the downwind pass increase. The result of this is seen in the performance drop during the upwind pass of the blade due to the lower angles of attack, and thus lower blade lift coefficients; and a performance increase on the downwind pass resulting from the slightly increased AOA and lift coefficients.

As β is decreased further, the power on the upwind pass continues to decrease, but it is now accompanied by a considerable reduction in performance on the downwind pass. When β is decreased to this point, the theoretical angles of attack on the downwind side

become so large that the blade stalls very sharply, and is in effect dragged around the remainder of its orbit. It should be mentioned also that the location of the peak torque on the upwind pass was not observed to vary significantly with changes in blade preset pitch.

As it is not desirable to be using extracted energy (by other turbine blades) to counteract negative torque due to drag on a blade, the preset pitch angle β should be very carefully chosen, since a very small change to the preset pitch angle from $-6°$ to $-9°$ resulted in drops in Cp of 12.4% and 18.4% for the NACA 0015 and NACA 0021 experimental results respectively.

CHAPTER 6: CONCLUSIONS AND RECOMMENDATIONS FOR FUTURE WORK

6.1 CONCLUSIONS

Performance testing of a high solidity vertical axis wind turbine was carried out in an open-air wind tunnel facility at the University of Waterloo in Ontario. The turbine used for these tests was a highly modified prototype of a small scale H-type commercial VAWT that was provided by the project's industrial partner Cleanfield Energy Inc.

Two separate wind tunnel test results have been presented. During the first series of preliminary tests, preset pitch configurations of +/-3.9° and +/-7.8° were tested and results show performance increases of up to 29% with a toe-out configuration. The value of tip speed ratio at peak power was observed to remain relatively constant for changes in preset pitch. These phenomena were observed for NACA 0015 and NACA 0021 blade profiles; however, the NACA 0021 profile resulted in improved performance over a broader range of tip speed ratios. In general, imposing a toe-in preset pitch resulted in dramatically decreased wind turbine performance, whereas toe-out preset pitch was seen to improve overall performance. Simple mount point offset tests were performed using blades with different mount locations. Observations conclude that offsetting the blade mount point location on a VAWT has an equivalent effect on performance as imposing a preset pitch to the airfoil. Therefore if the blade mount location is changed along the

chord line, it should be offset by the addition of a suitable preset pitch to avoid a decrease in performance.

During the more comprehensive series of wind tunnel tests, preset pitch configurations on both NACA 0015 and 0021 airfoils of β = *6°, 3°, 0°, -3°, -6°, -9°* and *-12°* were tested experimentally, along with blade mount point offsets of a = *53mm, 126.5mm, 273.5mm* and *347mm* (on 400mm chord airfoils). The results of the blade preset pitch experiments show performance increases up 18% with a near optimal toe-out blade configuration. Good agreement was observed when the mount point offset location was varied so as to impose a toe-in or toe-out condition that would be equivalent to having a mid-chord mount point and a given preset pitch. For a mid-chord mount point, the optimal preset pitch was around β = *-6°*. The value of the optimal tip speed ratio remained constant with changes in the blade pitch and offset but the peak of the *Cp* curve was observed to sharpen for preset pitches approaching the optimal value.

To help understand the aerodynamic effects of such pitch changes, tuft visualization on the inner blade surface was performed. Stall plots were created from tuft visualizations to describe the flow behaviour on the inner blade surface as the blade travels about its orbit. Increases in the blade tip speed ratio were observed to delay the onset of incipient stall and were accompanied by decreases in the overall duration the inner surface was experiencing fully reversed flow. The overall duration of the fully reversed flow region also decreases as β approaches the optimal value and then increases when the optimal value is exceeded.

2-D CFD simulations were performed on a NACA 0015 mid-chord mounted blade at $\beta = 0°$, $-3°$, $-6°$ and $-9°$. Poor agreement was observed between the 2-D simulations and the experimental power curves, as has been noticed recently by others; but were used here for determining trends. The predicted power curves for the $\beta = 0°$, $-3°$ and $-9°$ cases exhibited similar characteristics to the experimental curves, albeit at much higher tip speed ratios. Comparison of the performance curves indicated performance increases with increasing toe-out pitch up to $\beta = -6°$, which is consistent with the experimental findings. Stall plots generated from the CFD simulations showed relatively good agreement to the locations and durations of reversed flow seen in the tuft visualizations on the inner blade surface. Thrust curves indicated that as the tip speed ratio increased, the incipient stall location was delayed, and the vortices that were shed by the blade during the upwind pass and downwind pass were diminished. As increased amounts of toe-out were added, the peak thrust occurring on the upwind pass was observed to decrease while downwind pass performance was increased due to their respective ranges of angle of attack. It was concluded that while the 2-D nature of the simulations did not accurately predict actual absolute values of turbine performance, it is nevertheless a useful tool in observing general trends resulting from changes in turbine configuration.

6.2 Recommendations for Future Work

The rapidly fluctuating, three dimensional nature of the flow over VAWT blades cannot be modelled accurately with simplified 2-D models, making blade optimization a

difficult and time consuming process. All known H-Darrieus VAWTs use simple symmetrical blade profiles due to their simplicity of manufacturing and low cost. While these profiles may be adequate for low solidity turbines, significant performance improvements were gained with simple adjustments to the blade preset pitch and mount point offset for high solidity turbines, encouraging the investigation of asymmetric blade profiles. It follows that asymmetric blades could further increase performance with additional improvements. A first attempt at this may be performed by mapping out the effects of blade camber, which is similar to imposing a separate pitch to the leading and trailing edges of the blade. Due to the large number of tests required for this analysis, a batch of CFD simulations should be completed before new blades are constructed for wind tunnel testing.

The current CFD model does not predict absolute turbine performance adequately and therefore is only useful for observing general trends resulting from certain changes to turbine configuration. Ideally, the model would be expanded into a three dimensional model that would be able to account for flow above and below the turbine, as well as the effects of flow around the tips of the blades. This would, however, significantly increase the computational costs, and consequently the ability to do a wide range of simulations. Perhaps the use of a 3-D CFD model can be used to assess the validity of using a 2-D model to examine the detailed flow characteristics of a wider range of particular blade profiles.

A large amount of experimental results have been presented which can be used in future validation of a three dimensional model that could be used to further develop the turbine by investigating blade design, including planform blade variation; minimizing turbine vibrations due to periodic blade loading; and also studying the effects of turbine performance in spatially and temporally varying, 'dirty' airflows, such as those encountered in urban environments.

REFERENCES

Bravo, R., Tullis, S., & Ziada, S. (2007). *Performance Testing of a Small Vertical-Axis Wind Turbine.* Paper presented at the 21st Canadian Congress of Applied Mechanics Conference, Toronto, ON.

Cardona, J. L. (1984). Flow curvature and dynamic stall simulated with an aerodynamic free vortex model for VAWT. *Wind Energy, 8*(3), 135-143.

Cleanfield. (2009). Product Overview and Key Benefits. Retrieved August 10, 2009, from http://cleanfieldenergy.com/site/sub/p_we_overview.php

Fanucci, J. B., & Walter, R. E. (1976). *Innovative wind machines: The theoretical performance of a vertical-axis wind turbine.* Paper presented at the Vertical-Axis Wind Turbine Technology Workshop, Sandia Laboratories, USA.

Glauert, H. (1935). Windmills and fans. *Aerodynamic Theory, 4*, 324-341.

Guerri, O., Sakout, A., & Bouhadef, K. (2007). Simulations of the Fluid Flow around a rotating Vertical Axis Wind Turbine. *Wind Engineering, 31*(3), 149-163.

Hirsch, C., & Mandal, A. C. (1984, October 1984). *Flow Curvature Effects on Vertical Axis Darrieus Wind Turbines Having a High Chord-Radius Ratio.* Paper presented at the European Wind Energy Conference, Hamburg.

Holme, O. A. (1976). *Contribution to the aerodynamic theory of the vertical axis wind turbine.* Paper presented at the International symposium on wind energy systems, Cambridge, England.

Howell, R., Qin, N., Edwards, J., & Durrani, N. (2009). Wind tunnel and numerical study of a small vertical axis wind turbine. *Renewable Energy*.

Islam, M., Ting, D. S.-K., & Fartaj, A. (2007). Desirable Airfoil Features for Smaller-Capacity Straight-Bladed VAWT. *Wind Engineering, 31*(3), 165-196.

Jones, W. P., & Launder, B. E. (1972). The Prediction of Laminarization with a Two-Equation Model of Turbulence. *International Journal of Heat and Mass Transfer, 15*, 301-314.

Klimas, P., & Worstell, M. (1981). *Effects of Blade Preset Pitch/Offset on Curved-Blade Darrieus Vertical Axis Wind Turbine Performance* (No. SAND-81-1762). Albuquerque, NM: Sandia National Laboratories.

Kooiman, S. (2008). *Urban wind flow effects on the aerodynamic performance of a vertical axis wind turbine.* McMaster University, Hamilton, ON.

Larsen, H. C. (1975). *Summary of a vortex theory for the cyclogiro.* Paper presented at the Second US National Conference on Wind Engineering Research, Colorado State University.

Mandal, A. C., & Burton, J. D. (1994). The Effects of Dynamic Stall and Flow Curvature on the Aerodynamics of Darrieus Turbines Applying the Cascade Model. *Wind Engineering, 18*, 267-282.

McLaren, K., Tullis, S., & Ziada, S. (2007a, May, 2007). *CFD Simulation of Dynamic Thrust and Radial Forces on a Vertical Axis Wind Turbine Blade.* Paper presented at the 15th Annual CFD Society of Canada Conference, Toronto, ON.

McLaren, K., Tullis, S., & Ziada, S. (2007b). *Vibration Analysis of a Vertical Axis Wind Turbine Blade.* Paper presented at the 21st Canadian Congress of Applied Mechanics Conference, Toronto, ON.

McLaren, K., Tullis, S., & Ziada, S. (2009). CFD Simulation of the Performance of a High Solidity, Small Scale Vertical Axis Wind Turbine. *Submitted to Journal of Wind Engineering & Industrial Aerodynamics*.

Menter, F. R. (1992). Influence of freestream values on k-omega turbulence model predictions. *AIAA Journal, 30*(6), 1657-1659.

Menter, F. R. (1994). Two-equation Eddy-viscosity Turbulence Models for Engineering Applications. *AIAA Journal, 32*, 269-289.

Menter, F. R., Kuntz, M., & Langtry, R. (2003). Ten Years of Industrial Experience with the SST Turbulence Model. *Turbulence, Heat and Mass Transfer 4*.

Migliore, P. G., Wolfe, W. P., & Fanucci, J. B. (1980). Flow Curvature Effects on Darrieus Turbine Blade Aerodynamics. *Journal of Energy, 4*(2), 49-55.

Newman, B. G. (1983). Actuator-disk theory for vertical-axis wind turbines. *Journal of Wind Engineering and Industrial Aerodynamics, 15*, 347-355.

Paraschivoiu, I. (1983). Predicted and Experimental Aerodynamic Forces on the Darrieus Rotor. *AIAA Journal of Energy, 7*(6), 610-615.

Paraschivoiu, I. (1988). Double-multiple streamtube model for studying vertical-axis wind turbines. *Journal of Propulsion and Power, 4*(4), 370-377.

Paraschivoiu, I. (2002). *Wind Turbine Design with Emphasis on Darrieus Concept.* Montreal: Polytechnic International Press.

Paraschivoiu, I., & Delclaux, F. (1983). Double-Multiple Streamtube Model with Recent Improvements. *AIAA Journal of Energy, 7*(3), 250-255.

Sandia. (2008). Vertical Axis Wind Turbine: The History of the DOE Program. Retrieved August 10, 2008, from www.sandia.gov/wind/topical.htm#VAWTARCHIVE

Shankar, P. N. (1976). *On the Aerodynamic Performance of a Class of Vertical Shaft Windmills.* Paper presented at the Royal Society of London.

Sheldahl, R. E., & Klimas, P. C. (1978). *Four Aerodynamic Prediction Schemes for Vertical-Axis Wind Turbines: A Compendium.* Albuquerque: Sandia National Laboratories Unlimited Release.

Sheldahl, R. E., & Klimas, P. C. (1981). *Aerodynamic Characteristics of Seven Symmetrical Airfoil Sections Through 180-Degree Angle of Attack for Use in Aerodynamic Analysis of Vertical Axis Wind Turbines*. Albuquerque, NM: Sandia National Laboratories.

South, P., & Rangi, R. S. (1972). *A Wind Tunnel Investigation of a 14ft. Diameter Vertical Axis Windmill* (No. LTR-LA-105): National Aeronautical Establishment.

Spalart, P. R., & Allmaras, S. R. (1992). A One-Equation Turbulence Model for Aerodynamic Flows. *AIAA-Paper 92-0439, 1*, 5-21.

Strickland, J. H. (1975). *The Darrieus Turbine: A Performance Prediction Model Using Multiple Streamtubes*. Albuquerque: Sandia Laboratories.

Strickland, J. H., Webster, B. T., & Nguyen, T. (1979). A Vortex Model of the Darrieus Turbine: An Analytical and Experimental Study. *Journal of Fluids Engineering, 101*(4), 500-505.

van Kuik, G. A. M. (2007). The Lanchester-Betz Joukowsky Limit. *Wind Energy, 10*(3), 289-291.

Weisinger, J. (2004). *Characterization of the University of Waterloo live Fire Research Facility Wind Generation System.* University of Waterloo, Waterloo.

Wilcox, D. C. (1993). *Turbulence modelling for CFD.* La Canada, CA: DCW Industries.

Wilson, R. E. (1980). Wind-turbine aerodynamics. *Journal of Wind Engineering and Industrial Aerodynamics, 5*(3-4), 357-372.

APPENDIX A: TURBINE LOSSES

Quantifying the wind turbine frictional and drag losses is important in order to accurately compare experimental turbine data for various turbine configurations, and to relate lossless CFD turbine performance to actual experimental results. Losses present in the Cleanfield V3.5 VAWT turbine setup include first order friction losses in the generator and shaft bearings, the motor freewheel assembly and the belt drive, and third order aerodynamic losses from the blades, struts, and any additional blade mounting devices (such as blade pitch/offset adapters).

Traditionally, the method used to quantify these losses was to measure the dynamic response of the turbine without the presence of a driving force. This was accomplished by spinning up the turbine (with blades attached) to a known angular velocity with the motor, and recording the amount of time required for it to come to a stop. Then a known mass was applied to the system, and the spin-down procedure was repeated. A simple analysis using Newton's second law of rotational motion allows for the determination of the turbine inertia, I, about the rotational axis. A complete explanation of the procedure is outlined in Kooiman (2008).

Certain difficulties were encountered when determining the losses using the aforementioned procedure. First, the losses due to the blade drag should not be included in the turbine loss calculation since they are a function of the angle of attack which is constantly fluctuating when the turbine is in operation. The blades were however left

attached for the spin-down tests to provide a mounting surface for the known masses that were used to alter the turbine inertia.

Secondly, the maximum angular velocity attainable by driving the turbine with the available electric motor was significantly lower than the nominal operating angular velocity. While this is not necessarily a problem, a more accurate loss calculation can be made if the turbine was to spin down over a larger range of angular velocities. The blades were replaced with flat steel bars of equivalent mass in order to minimize the drag, and increase the maximum angular velocity threshold however, visual observations of the rotating turbine indicated the steel bars were bulging outwards due to the centrifugal loads as the turbine was rotating, effectively varying the turbine geometry and inertia.

Lastly, a minimum of three spin-downs were required to determine the turbine inertia (one spin-down of the turbine in its usual configuration, one with boxes which will hold the additional masses, and a third with boxes and weights); a process which takes approximately 30 minutes. Additional spin downs would be necessary in order to achieve satisfactory average turbine inertia to calculate the losses. Finally, any time the turbine shaft or struts were changed, the losses would have to be recalculated; a very time consuming process.

A new method of calculating the turbine losses was developed which allowed for direct calculation of a turbine loss curve in approximately 10 minutes, allowing for the calculation of a new loss curve with every change in turbine configuration with very little turbine down-time. The turbine losses were calculated by determining the electrical

power required by the motor to drive the turbine at various angular velocities and subtracting the electrical losses of the motor. The procedure is relatively straight forward, requiring only a voltmeter and an ammeter to be connected to the DC motor controller to measure the voltage and current being supplied to the motor. When a stable turbine angular velocity is reached, and the voltage and current readings have stabilized on the multi-meters, the data is recorded, and the angular velocity is subsequently increased. The test is performed without the turbine blades, allowing for a realistic calculation of turbine friction and drag losses. Also, the floating brake caliper is removed from the turbine since the energy lost as friction in the brake caliper is already accounted for directly by the load cell measurements during regular turbine operation.

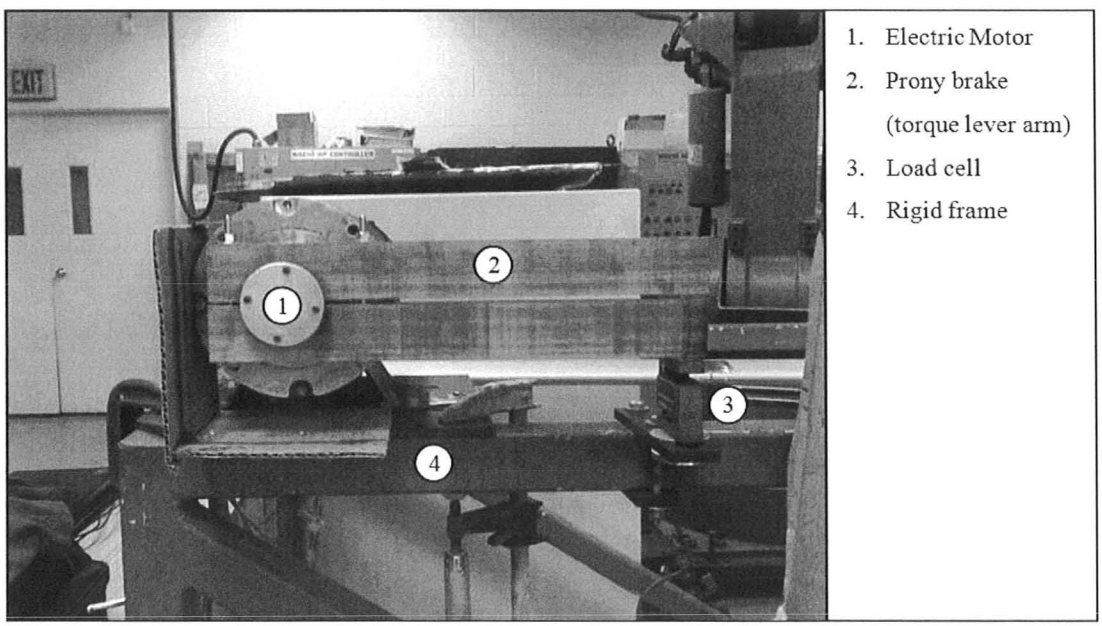

Figure 8-1: Front view of simple prony brake setup to determine DC motor losses.

The DC motor efficiency that is provided on the name plate of the motor is only applicable at the design speed of the motor, and because the motor was being operated at

a much lower speed range, a motor efficiency curve had to be calculated. This was accomplished by means of a simple prony-brake dynamometer using the same load cell employed on the turbine. The motor voltage and current were measured as before, the torque was measured using the load cell and a prony-brake lever arm, while the motor speed was measured using an optical tachometer. Torque was applied to the motor such that the voltage and current readings were similar to those experienced during turbine loss calculations. The linear relationship that exists between motor torque and current for permanent magnet electric motors, known as the torque constant, K_t, was thus determined. It follows that the DC motor efficiency is given by:

$$\epsilon_{motor} = C_1 \frac{K_t \omega_{turb}}{V} \tag{8-1}$$

where K_t is the motor torque constant, ω_{turb} is the turbine angular velocity, V is the supplied voltage to the motor, and C_1 is the ratio of the generator diameter to the diameter of the motor pulley and is equal to 5.0.

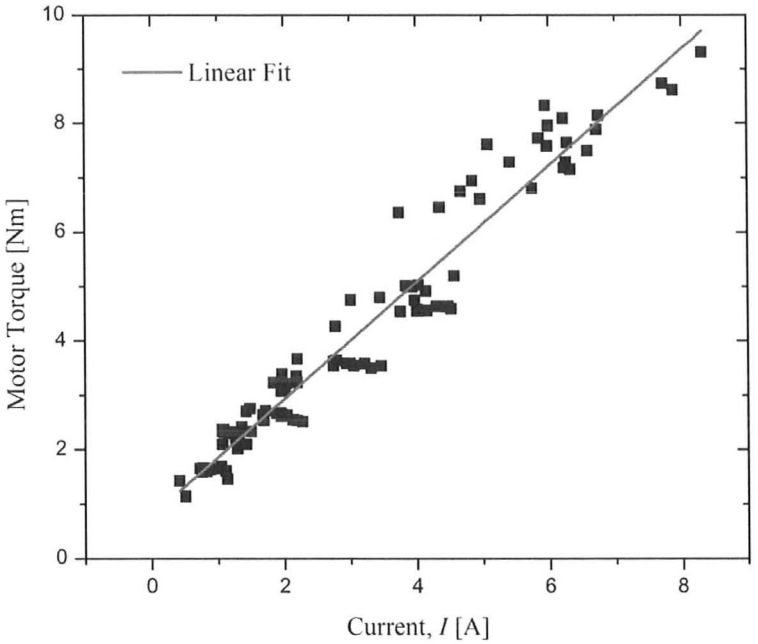

Figure 8-2: Relationship between motor torque and current for Leeson 2HP DC permanent magnet motor.

By applying the appropriate motor efficiency value based on the voltage and current drawn by the motor at a particular turbine speed, the frictional and aerodynamic loss curves for various turbine configurations, like the one in Figure 4-8, were created and the experimental results were modified accordingly.